# Open quantum maps from complex scaling of kicked scattering systems

Normann Mertig and Akira Shudo
*Department of Physics, Tokyo Metropolitan University, Minami-Osawa, Hachioji 192-0397, Japan*

(Received 5 September 2017; published 25 April 2018)

We derive open quantum maps from periodically kicked scattering systems and discuss the computation of their resonance spectra in terms of theoretically grounded methods, such as complex scaling and sufficiently weak absorbing potentials. In contrast, we also show that current implementations of open quantum maps, based on strong absorptive or even projective openings, fail to produce the resonance spectra of kicked scattering systems. This comparison pinpoints flaws in current implementations of open quantum maps, namely, the inability to separate resonance eigenvalues from the continuum as well as the presence of diffraction effects due to strong absorption. The reported deviations from the true resonance spectra appear, even if the openings do not affect the classical trapped set, and become appreciable for shorter-lived resonances, e.g., those associated with chaotic orbits. This makes the open quantum maps, which we derive in this paper, a valuable alternative for future explorations of quantum-chaotic scattering systems, for example, in the context of the fractal Weyl law. The results are illustrated for a quantum map model whose classical dynamics exhibits key features of ionization and a trapped set which is organized by a topological horseshoe.

DOI: 10.1103/PhysRevE.97.042216

## I. INTRODUCTION

Recent decades have witnessed significant progress in the semiclassical understanding of resonance states and resonance spectra of complex scattering systems. In particular, for scattering systems with fully chaotic dynamics it was explored (i) how scattering from a chaotic repeller can lead to the formation of a spectral gap [1–3], (ii) how properties of the classical dynamics are reflected in the fluctuations of the scattering matrix [4–8], (iii) how resonance eigenvalues can be determined from periodic orbits [9,10], (iv) how counting functions of long-lived resonance states relate to the fractal dimension of the classical invariant sets (fractal Weyl law) [11–17], and (v) how resonance states localize on classical invariant sets [18,19].

In order to corroborate and extend such results, it is crucial to have good toy models. Ideally, such toy models should be easy to exploit numerically and yet generic enough to exhibit a robust effect of quantum-to-classical correspondence. Toy models which are believed to exhibit these properties are open quantum maps; see Ref. [20] for their mathematical definition, Refs. [15,16] for reviews, and Refs. [14–19,21–41] for examples.

In theory, open quantum maps quantize the classical flow of an open system along its trapped set and represent a reduction of the corresponding scattering system to a subunitary operator, which holds the essential information on long-lived resonances [15,20,42]. In a similar spirit [43], one may think of open quantum maps as the time-evolution operator corresponding to an effective Hamiltonian which arises from a reduction of a scattering system via the Feshbach approach [44–46]. Altogether, this shows that the concept of open quantum maps rests upon a firm theoretical foundation. Hence, it is not surprising that open quantum maps have been used to model all sorts of scattering systems, such as ionizing atoms [21], mesoscopic scattering systems with point contacts [24–28] in a spirit similar to random matrix theory [47,48], or dielectric cavities [32,38].

In spite of their firm theoretical background and popularity, there remains room for criticism when it comes to practical implementations of open quantum maps, which we refer to as heuristic models throughout this paper. One criticism is that none of the aforementioned theoretical approaches has ever been used to derive an open quantum map from a concrete scattering system. Instead, virtually any known open quantum map is a heuristic model which is introduced in an *ad hoc* manner by combining the unitary time-evolution operator of a closed system, such as a quantum map on a torus, with an absorption operator, such as a Fresnel-type reflection operator or a projector (see Refs. [14–19,21–41] for examples). While these heuristic models have stimulated many findings in the past, they do not represent a step by step reduction of a scattering system in the sense of Ref. [20] and it remains unclear to what degree they faithfully represent resonances.

Another criticism of heuristic models centers around the somewhat distracting use of nonanalytic absorption operators for the following reasons. (i) The reduction of scattering systems to open quantum maps as described in Ref. [15] explicitly excludes nonanalytic absorption operators. (ii) In quantum chemistry computations of resonance spectra based on absorbing potentials, one carefully has to minimize the backreflections from absorbing potentials into the scattering region [49]. In such cases rapidly varying absorbing potentials with nonanalytic parts obscure the computation. (iii) Scattering systems with nonanalytic potentials usually exhibit diffraction effects which make quantitative investigations of quantum-to-classical correspondence considerably more complicated [50–52]. All in all this makes quantum map models of scattering based on analytic potentials desirable.

In this paper we propose a class of open quantum maps which is not hampered by the foregoing criticism. This class

 

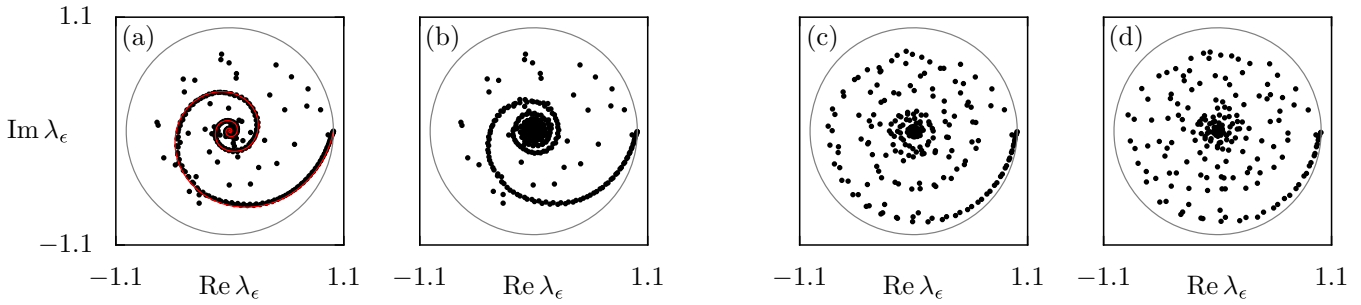


FIG. 1. Numerically determined spectra (dots) of a kicked scattering system for kick strength $\kappa = 11$ (chaotic dynamics) and effective Planck constant $h_{\text{eff}} = 1/50$. See the text for details. The gray line represents a unit circle. The resonance spectrum separates from the continuous spectrum for (a) complex scaling and (b) weak absorbing potentials. The continuous spectrum localizes along a spiral [red line in (a)]. Numerical spectra are obtained with (c) strong absorbing potentials and (d) projective openings. The separation of continuous and resonance spectra is lost.

of open quantum maps derives from periodically kicked scattering systems with analytic potentials and describes the time evolution of these systems. In contrast to heuristic models, the quantum maps of kicked systems will naturally accommodate resonances and do not require adding any absorption to the system. In particular, the clear connection with periodically kicked scattering systems allows for applying the method of complex scaling [53–57] as previously developed for time-periodic systems [58–62]. This results in a complex-scaled quantum map (48), from which the resonance spectra of kicked scattering systems can readily be computed in a mathematically rigorous manner [see Fig. 1(a) for an example].

In this paper we further examine to what degree the framework of heuristic models allows for computing resonance spectra. To this end we adapt the method of absorbing potentials [49] to kicked scattering systems. This results in an absorption-augmented quantum map (54), which has exactly the same structure as heuristic model systems. We show that this quantum map also allows for computing the resonance spectrum of kicked scattering systems, albeit only in the limit of sufficiently weak absorption [see Fig. 1(b)]. On the other hand, we demonstrate that strong absorbing potentials and projective openings, as commonly used for heuristic models, do not allow for computing the resonance spectrum of kicked scattering systems [see Figs. 1(c) and 1(d), respectively].

In comparing heuristic models with strong absorptive and projective openings to theoretically grounded methods such as complex scaling and weak absorption, our results demonstrate major deficiencies in heuristic models. (i) A real scattering system will always exhibit a continuous spectrum which must be carefully separated from the resonance spectrum in numerical computations [49,57]. In kicked scattering systems this separation can be accomplished by means of complex scaling and weak absorbing potentials. For an illustration see Figs. 1(a) and 1(b), where the continuous spectrum is located along a spiral, while resonance eigenvalues can be found away from the spiral. On the other hand, upon increasing the absorption towards either strong absorptive or even projective openings, we observe a blowup of the continuous spectrum [see Figs. 1(c) and 1(d)]. As a consequence, the accuracy of the eigenvalues degrades and it becomes impossible to separate resonance eigenvalues from remnants of the continuous spectrum. We emphasize that this problem occurs even if the absorption does not affect the trapped set, which carries the semiclassical information on the resonance spectrum. All in all, this obscures the meaning of resonance eigenvalues in heuristic models.

(ii) Our results hint at the presence of diffraction in heuristic models. That is, in contrasting resonance spectra as obtained from complex scaling, on the one hand, with resonance spectra as obtained from strong absorptive or projective openings, on the other hand, we present two implementations of kicked scattering systems whose classical trapped sets are identical. In such circumstances one would semiclassically expect from periodic orbit theory that any implementation should have identical resonance spectra. Thus, the spectral discrepancy between both implementations hints at the presence of nonclassical diffraction effects, presumably due to nonanalytic absorbing potentials in heuristic model systems.

In summary, the results of this paper cast doubt on the utility of heuristic models for explorations of quantum chaotic scattering systems. In particular, our results question to what degree heuristic models, such as the open baker's map and the open standard map, can be trusted when exploring spectral properties of chaotic scattering systems, such as the fractal Weyl law.

In order to illustrate our results and further establish the utility of our class of open quantum maps for explorations of chaotic scattering, we introduce a model system whose kicking potential is composed of entire functions. For this model system we discuss the organization of its classical flow in terms of few stable and unstable manifolds, following standard methods in Hamiltonian transport [63–67]. This discussion shows that kicked scattering systems exhibit the same phase-space structures which commonly appear in classical ionization [68–70] and dissociation [71]. Moreover, it allows for demonstrating that the trapped set of our model system is organized in a topological horseshoe.

Ultimately, we hope that the quantum maps of kicked scattering systems which we present in this paper can become a viable alternative to heuristic models. To this end it would be useful if the uniform hyperbolicity of the proposed model system can be proven. This would result in a uniformly hyperbolic model system, which, in contrast to the three-disk

scatterer [1–3,72] and the open baker's map [15,29–31,33], is free from distracting diffraction effects. This should be useful for future investigations of the fractal Weyl conjecture and further topics in chaotic scattering. Even more so, we expect that the quantum maps of kicked scattering systems should be useful for exploiting scattering systems with a mixed phase space, for which many more questions of quantum-to-classical correspondence remain unsolved.

The paper is organized as follows. In Sec. II we specify periodically kicked scattering systems and lay out some basic notation. In Sec. III we introduce the model system and discuss its classical dynamics. In Sec. IV we derive quantum maps for periodically kicked scattering systems and discuss the computation of their resonance spectra in terms of complex scaling and absorbing potentials. A summary and discussion are given in Sec. V. The numerical computations are documented in the Appendixes.

## II. KICKED SCATTERING SYSTEMS

In this paper we are concerned with periodically kicked, one-degree-of-freedom quantum systems which obey the time-dependent Schrödinger equation

$$\left[i\hbar\frac{\partial}{\partial t}+\frac{\hbar^2}{2}\frac{\partial^2}{\partial q^2}-V(q)\sum_{n\in\mathbb{Z}}\delta(t-n)\right]\psi(q,t)=0. \tag{1}$$

Here all quantities have been scaled to dimensionless units. In particular, $q\in\mathbb{R}$ denotes the position, $t\in\mathbb{R}$ denotes time, $\hbar\in\mathbb{R}^+$ denotes the reduced effective Planck constant, and $\psi$ represents the wave function. We further refer to $h_{\mathrm{eff}}:=2\pi\hbar$ as the effective Planck constant. It is treated as a free parameter and $h_{\mathrm{eff}}\to 0$ denotes the semiclassical limit. Furthermore, $\delta(\cdot)$ represents the Dirac $\delta$ function. The corresponding classical dynamics is given by the Hamilton function

$$H(q,p;t)=\frac{p^2}{2}+V(q)\sum_{n\in\mathbb{Z}}\delta(t-n), \tag{2}$$

with $p\in\mathbb{R}$ being the momentum. The crucial point of this paper is to consider kicking potentials $V(q)$ which tend to zero sufficiently fast as $|q|$ tends to infinity

$$\lim_{q\to\pm\infty}V(q)=0, \tag{3}$$

i.e., we consider scattering systems for which the classical dynamics resemble free motion as $|q|$ tends to infinity.

*Classical map.* In order to investigate the classical dynamics of periodically kicked scattering systems we use stroboscopic phase-space sections. They are obtained by integrating Hamilton's equations of motion over one period in time. This results in a symplectic map on $\mathbb{R}^2$,

$$U:(q_n,p_n)\mapsto(q_{n+1},p_{n+1}), \tag{4}$$

which in its symmetrized version is given by

$$q_{n+1}=q_n+p_n-\tfrac{1}{2}V'(q_n), \tag{5a}$$

$$p_{n+1}=p_n-\tfrac{1}{2}V'(q_n)-\tfrac{1}{2}V'(q_{n+1}). \tag{5b}$$

Here $(q_n,p_n)$ denotes phase-space points along a trajectory in the middle of the $n$th kick, while $V'$ denotes the derivative of the kicking potential with respect to $q$.

*Quantum map.* The quantum mechanical analog of the classical map $U$ is the time-evolution operator over one period of the external driving [73,74]. This operator is referred to as a quantum map [73]. It is given by

$$\hat{U}=\exp\left(-\frac{i}{\hbar}\frac{V(\hat{q})}{2}\right)\exp\left(-\frac{i}{\hbar}\frac{\hat{p}^2}{2}\right)\exp\left(-\frac{i}{\hbar}\frac{V(\hat{q})}{2}\right), \tag{6}$$

where the operators fulfill the usual commutation relation $[\hat{q},\hat{p}]=i\hbar$. Due to Eq. (3), the system is unbound and the quantum map supports a resonance spectrum. Thus, it is already open. In order to access its resonance spectrum we will derive its complex-scaled form, Eq. (48), and its absorption-augmented form, Eq. (54).

## III. MODEL SYSTEM: CLASSICAL DYNAMICS

In this section we specify the model system and discuss its classical dynamics.

### A. A family of kicking potentials

In what follows we consider maps induced by the kicking potential

$$V(q)=V_\kappa(q)+V_\epsilon(q). \tag{7}$$

Its main part is an attractive Gaussian

$$V_\kappa(q)=-\frac{\kappa}{16}\exp(-8q^2), \tag{8}$$

with kick strength $\kappa\geqslant 0$. This system was previously studied as a model of chaotic scattering [75,76] as well as a model of a pulsed optical trap for cold-atom systems [77]. For $\kappa<0$ it has further been used as a model of an oscillating barrier potential [78,79]. The dimensionless units are chosen such that a version of Chirikov's standard map [80], induced by $V(q)=-\kappa/(2\pi)^2\cos(2\pi q)$, is mimicked in the region $q\in(-0.5,0.5)$. This applies in particular to the stability matrix which controls the dynamics around the central fixed point $(q_c,p_c)=(0,0)$ as well as the extrema of $V'(q)$, located at $q_e=\pm 1/4$.

In order to confine the trapped set of the model system in a compact region, we further add a perturbation term. This perturbation term could be any function, which ensures that the overall potential in Eq. (7) decreases to zero monotonically in the asymptotic regions ($q\to\pm\infty$). Since we do not expect the conclusions of this paper to crucially depend upon the details of the perturbation term, we make the convenient choice

$$V_\epsilon(q)=-\epsilon\{\mathrm{erf}(\sqrt{8}[q-x_b])-\mathrm{erf}(\sqrt{8}[q+x_b])\}, \tag{9}$$

where $\mathrm{erf}(\cdot)$ is the error function, $x_b$ is a positive real parameter, and $\epsilon>0$ is a small perturbation strength determined as

$$\epsilon=\frac{\kappa\sqrt{\pi}}{2\sqrt{8}}x_f\frac{\exp(-8x_b[2x_f-x_b])}{1-\exp(-32x_fx_b)}, \tag{10}$$

with

$$16x_bx_f>1. \tag{11}$$

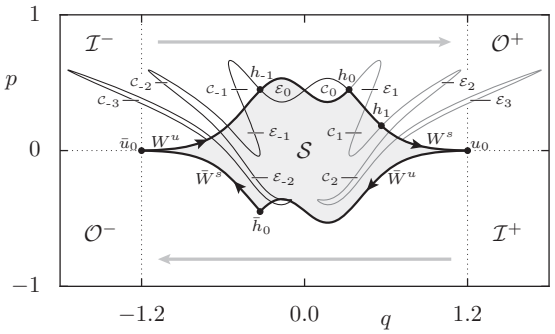


FIG. 2. Phase space of the model system for $\kappa = 2.9$. The initial segments of the stable and unstable manifolds (thick lines) form the boundary of the (gray shaded) scattering region. Dots represent fixed points and heteroclinic points. Thin lines show the stable (black) and unstable (gray) manifolds, which form the boundary of the lobe areas. Gray arrows indicate transport from incoming to outgoing regions, as marked by dotted lines.

This choice is motivated as follows. (i) The functional form of the perturbation term is convenient for comparing the derivatives of Eqs. (8) and (9), which explains the factor $\sqrt{8}$ in Eq (9). This is useful for proving that the overall potential decreases monotonically in the asymptotic regions ($q \to \pm\infty$). (ii) The above perturbation term confines the trapped set to the strip $(q,p) \in [-x_\mathrm{f},x_\mathrm{f}] \times \mathbb{R}$ and Eq. (10) allows for directly controlling the perturbation strength $\epsilon$ through the width $x_\mathrm{f}$ of that strip. (iii) Finally, Eq. (11) is a sufficient condition, which allows for proving the confinement of the trapped set. See Appendix A and the discussion below for details.

More specifically, for the above perturbation term, it can be proven that any trajectory entering the outgoing regions

$$\mathcal{O}^+ = \{(q,p) \in \mathbb{R}^2 : p > 0, q > x_\mathrm{f}\}, \tag{12}$$

$$\mathcal{O}^- = \{(q,p) \in \mathbb{R}^2 : p < 0, q < -x_\mathrm{f}\} \tag{13}$$

escapes to $q \to \pm\infty$, respectively. Due to time-reversal symmetry, this further gives the incoming regions

$$\mathcal{I}^+ = \{(q,p) \in \mathbb{R}^2 : p < 0, q > x_\mathrm{f}\}, \tag{14}$$

$$\mathcal{I}^- = \{(q,p) \in \mathbb{R}^2 : p > 0, q < -x_\mathrm{f}\}, \tag{15}$$

where trajectories escape to $q \to \pm\infty$ in backward time (see Fig. 2 for a sketch and Appendix A for details). Thus, the perturbation term ensures that the trapped set

$$\mathcal{K} := \left\{(q,p) \in \mathbb{R}^2 : \lim_{n\to\pm\infty} |U^n(q,p)| < \infty\right\} \tag{16}$$

is confined to the strip $(q,p) \in [-x_\mathrm{f},x_\mathrm{f}] \times \mathbb{R}$. Furthermore, one can show that the trapped set must be contained in a compact square

$$\mathcal{K} \subset [-x_\mathrm{f},x_\mathrm{f}] \times [-p_\mathrm{max},p_\mathrm{max}]. \tag{17}$$

Here $p_\mathrm{max}$ must be chosen sufficiently large such that any point with $q \in [-x_\mathrm{f},x_\mathrm{f}]$ and $|p| > p_\mathrm{max}$ has sufficient momentum to reach either of the outgoing regions $\mathcal{O}^\pm$ in one iteration of the map $U$. Since $V'(q)$ is bounded, a valid choice is given by $p_\mathrm{max} = 2x_\mathrm{f} + \max_{q\in\mathbb{R}}\{V'(q)\}$.

The above choice of parameters [Eqs. (10) and (11)] further allows for locating two unstable fixed points at

$$u_0 := (x_\mathrm{f},0), \quad \bar{u}_0 := (-x_\mathrm{f},0). \tag{18}$$

As discussed in the next section, their stable and unstable manifolds control the dynamics in the scattering region and provide sharper bounds on the trapped set.

Note that the proposed kicking potential fulfills Eq. (3). In fact, it decreases to zero exponentially fast and drops below machine precision for $|q| \gtrsim 2$. It further is an entire function, i.e., it has no discontinuities.

### B. Phase space

From now on we fix the parameters of the model system as $x_\mathrm{f} = 1.2$ and $x_\mathrm{b} = 1$ and discuss its phase space.

#### *1. Scattering region*

In this section we discuss how the stable and unstable manifolds of the fixed points $u_0$ and $\bar{u}_0$ organize the classical dynamics. The discussion follows standard arguments in classical transport [63–67] and commonly appears in problems of classical ionization [68–70] and dissociation [71]. The discussion is visually supported by Fig. 2 for the example $\kappa = 2.9$. Qualitatively similar structures are observed for any $\kappa > 0$.

In what follows we omit manifolds which trivially extend into the outgoing and incoming regions. We further focus on one side of the symmetry. Related properties for the symmetry partners, as marked by an overbar, are implied. We refer to the stable manifold of $u_0$ as $W^s$ and the unstable manifold of $\bar{u}_0$ as $W^u$. A closed segment of a manifold $W$ with end points $x$ and $x'$ is referred to as $W[x,x']$.

*a. Initial segments.* We start by numerically constructing the initial segments of the relevant manifolds up to their first heteroclinic intersection points $h_0$ and $\bar{h}_0$. Here $h_0$ is chosen such that

$$W^u[\bar{u}_0,h_0] \cap W^s[h_0,u_0] = h_0. \tag{19}$$

Note that $h_0$ gives rise to a heteroclinic orbit and replacing it by any of its forward or backward iterates is a topologically equivalent choice. The example system exhibits two distinct heteroclinic orbits whose points satisfy condition (19). Here we choose $h_0$ from the heteroclinic orbit which has no point along the symmetry axis $q = 0$. This choice is convenient in the discussion of the topological horseshoe further below.

*b. Scattering region.* We now define the scattering region $\mathcal{S}$. It is the compact set whose boundary is given by the closed curve of initial segments

$$\partial\mathcal{S} = W^u[\bar{u}_0,h_0] \cup W^s[h_0,u_0] \cup \bar{W}^u[u_0,\bar{h}_0] \cup \bar{W}^s[\bar{h}_0,\bar{u}_0]$$

(see the thick lines and the gray shaded region in Fig. 2).

*c. Lobes.* In the next step we consider a backward iteration of the map $U$. This maps the heteroclinic point $h_0$ onto $h_{-1}$. It further shortens the initial segment of the unstable manifold to the point $h_{-1}$. The initial segment of the stable manifold

reproduces up to the point $h_0$ and produces an additional segment $W^s[h_0,h_{-1}]$. This segment and the segment $W^u[h_0,h_{-1}]$ together form the boundary of two lobes, labeled $\mathcal{E}_0$ and $\mathcal{C}_0$ in Fig. 2. To be precise, $\mathcal{E}_0$ includes boundary points which are not on the stable segment, while $\mathcal{C}_0$ includes boundary points which are not on the unstable segment. Propagating the lobes and the corresponding segments of the stable and unstable manifolds forward and backward to times $i \in \mathbb{Z}$ gives the lobe iterates, according to

$$\mathcal{C}_i = \{(q,p) \in \mathbb{R}^2 : U^{-i}(q,p) \in \mathcal{C}_0\}, \tag{20a}$$

$$\mathcal{E}_i = \{(q,p) \in \mathbb{R}^2 : U^{-i}(q,p) \in \mathcal{E}_0\}. \tag{20b}$$

This is depicted in Fig. 2.

*d. Partial barrier, flux, and turnstiles.* As discussed in Refs. [63,64,66], the curve $W^u[\bar{u}_0,h_0] \cap W^s[h_0,u_0]$ is a partial barrier. Orbits which leave the scattering region across the partial barrier in one iteration of the map are initially in $\mathcal{E}_0$ and map to $\mathcal{E}_1$. Orbits which enter the scattering region across the partial barrier in one iteration of the map are initially in $\mathcal{C}_0$ and map to $\mathcal{C}_1$. The Lebesgue measure $\mu(\cdot)$ of all lobes is equal to

$$\Phi := \mu(\mathcal{E}_i) = \mu(\mathcal{C}_i) \quad \forall i \in \mathbb{Z}$$

such that $\Phi$ denotes the flux exchanged across the partial barrier in one iteration of the map. This mechanism is called turnstile transport.

*e. No return, escape, and capture.* The model system exhibits additional properties, which commonly appear in classical ionization [68,69] and dissociation [71]. Namely, after leaving the scattering region the $\mathcal{E}$ lobes do not return and propagate into the outgoing region

$$\mathcal{S} \cap \mathcal{E}_{i>0} = \emptyset, \quad \lim_{i\to\infty} \mathcal{E}_i \subset \mathcal{O}^+. \tag{21}$$

Hence, we call them escape lobes. Similarly, after leaving the scattering region in backward time the $\mathcal{C}$ lobes do not return and propagate into the incoming region

$$\mathcal{S} \cap \mathcal{C}_{i\leqslant 0} = \emptyset, \quad \lim_{i\to-\infty} \mathcal{C}_i \subset \mathcal{I}^-. \tag{22}$$

Since any orbit propagating from an incoming region into the scattering region must pass through $\mathcal{C}_0$, we call them capture lobes.

*f. Trapped set.* The above properties imply that the trapped set $\mathcal{K}$ is confined to the scattering region as

$$\mathcal{K} \subset \mathcal{S} \setminus \cup_{i\in\mathbb{Z}}(\mathcal{C}_i \cup \mathcal{E}_i \cup \bar{\mathcal{C}}_i \cup \bar{\mathcal{E}}_i). \tag{23}$$

This is because any orbit of the model system which is neither on a capture lobe nor within the scattering region trivially propagates towards the outgoing region. Hence, the trapped set must be on the capture lobes or within the scattering region. Further, excluding both escape and capture lobes, due to Eqs. (21) and (22), gives the above property.

*g. Dynamics in the scattering region.* For intermediate kick strength ($1 \lesssim \kappa \lesssim 6$) the dynamics in the scattering region exhibit a mixed phase space. Here the trapped set $\mathcal{K}$ accommodates regular motion along invariant tori. As the kicking strength of the model system is increased beyond $\kappa \gtrsim 8$, we are no longer able to detect regular motion in numerical simulations. In particular, when searching for periodic orbits up to period ten, we find all of the numerically detected orbits to be unstable. The dynamics in the scattering region becomes chaotic.

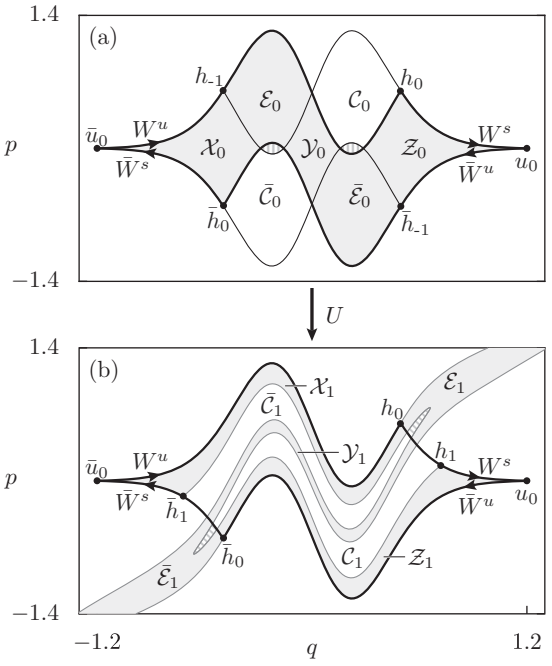


FIG. 3. (a) Scattering region and (b) its forward iterate (gray areas), for $\kappa = 11$. Lines represent the stable and unstable manifolds of the fixed points $u_0$ and $\bar{u}_0$. Dots denote fixed points and heteroclinic points. Gray striped regions indicate the nonempty intersections (27).

### 2. *Topological horseshoe*

In this section we present numerical evidence that the scattering region turns into a topological horseshoe for kick strength $\kappa \gtrsim 10.5$. We start by considering the forward and backward iterates of the scattering region $\mathcal{S}$, as illustrated in Figs. 3 and 4 for $\kappa = 11$. Here the forward iterate of the scattering region $U(\mathcal{S})$ cuts across the scattering region $\mathcal{S}$ along three mutually disjoint sets $\mathcal{X}_1$, $\mathcal{Y}_1$, and $\mathcal{Z}_1$,

$$\mathcal{S} \cap U(\mathcal{S}) = \mathcal{X}_1 \cup \mathcal{Y}_1 \cup \mathcal{Z}_1. \tag{24}$$

The rest of the forward iterate $U(\mathcal{S})$ is located along the escape lobes $\mathcal{E}_1$ and $\bar{\mathcal{E}}_1$, which do not return to the scattering region (see Fig. 3). Similarly, the backward iterate of the scattering region $U^{-1}(\mathcal{S})$ cuts across the scattering region $\mathcal{S}$ along three mutually disjoint sets $\mathcal{X}_0$, $\mathcal{Y}_0$, and $\mathcal{Z}_0$,

$$\mathcal{S} \cap U^{-1}(\mathcal{S}) = \mathcal{X}_0 \cup \mathcal{Y}_0 \cup \mathcal{Z}_0. \tag{25}$$

The rest of the backward iterate is located along the capture lobes $\mathcal{C}_0$ and $\bar{\mathcal{C}}_0$, which do not return to the scattering region in backward time (see Fig. 4). This is a topological horseshoe.

In order to show the structure of the topological horseshoe more clearly, we summarize the foregoing discussion in a homeomorphically equivalent schematic representation in Fig. 5. Here the scattering region appears as a square in a plane. Furthermore, any point which leaves the square, in either forward or backward time, tends to infinity and never returns. The forward and backward iterates of the scattering region are

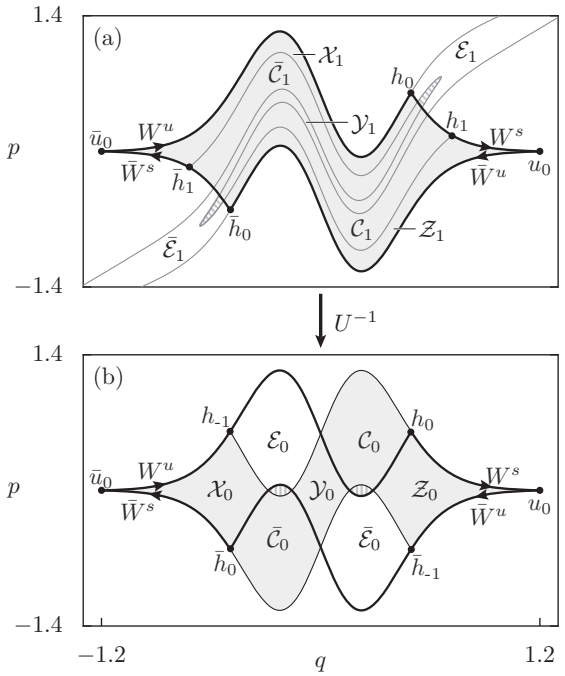


FIG. 4. (a) Scattering region and (b) its backward iterate (gray areas), for $\kappa = 11$. Lines represent the stable and unstable manifolds of the fixed points $u_0$ and $\bar{u}_0$. Dots denote fixed points and heteroclinic points. Gray striped regions indicate the nonempty intersections (27).

cut in three mutually disjoint vertical and horizontal stripes, thus forming a topological horseshoe.

We remark that the topological horseshoe for this model is realized through a phenomenon reminiscent of the first tangency in the Hénon map. Namely, for the model system, we

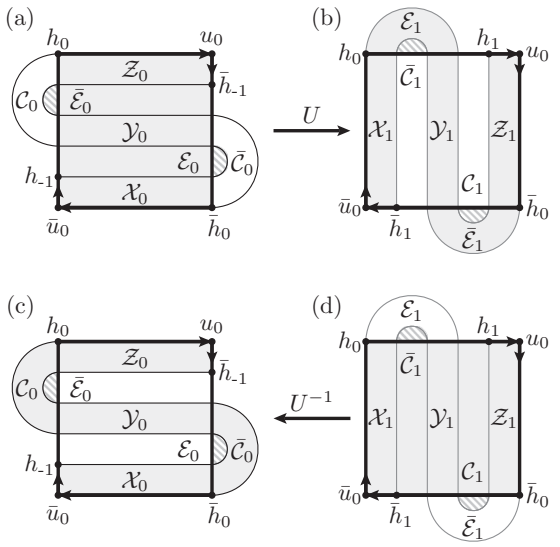


FIG. 5. (a) and (d) The scattering region and (b) its forward and (c) backward iterates, respectively, are schematically shown by gray areas. Lines represent the stable and unstable manifolds of the fixed points $u_0$ and $\bar{u}_0$. Dots represent fixed points and heteroclinic points. Gray striped regions indicate the nonempty intersections (27).

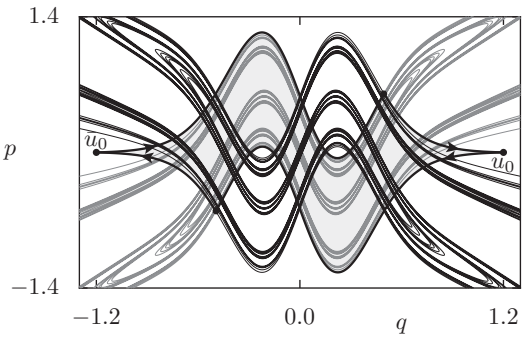


FIG. 6. Stable and unstable manifolds of the fixed points $u_0$ and $\bar{u}_0$ for $\kappa = 11$ are depicted by gray and black lines, respectively. The initial segments (thick lines) form the boundaries of the (gray shaded) scattering region.

find that the scattering region turns into a topological horseshoe if the lobes have nonempty intersections

$$\mathcal{E}_0 \cap \bar{\mathcal{C}}_0 \neq \emptyset, \quad \bar{\mathcal{E}}_0 \cap \mathcal{C}_0 \neq \emptyset, \tag{26}$$

more specifically, if the corresponding boundary segments of the stable and unstable manifolds intersect transversally in exactly two homoclinic points. Combining Eq. (26) with Eq. (20) immediately implies that

$$\mathcal{E}_i \cap \bar{\mathcal{C}}_i \neq \emptyset, \quad \bar{\mathcal{E}}_i \cap \mathcal{C}_i \neq \emptyset \quad \forall i \in \mathbb{Z}. \tag{27}$$

Thus, the nonempty intersections (26) enforce that the capture lobes $\bar{\mathcal{C}}_1$ and $\mathcal{C}_1$ are pulled through the scattering region in a forward iteration. These capture lobes cut the remaining part of the scattering region into three disjoint stripes, thus enforcing a topological horseshoe. For an illustration, see Figs. 3, 5(a), and 5(b), where the nonempty intersections in Eq. (27) are marked by gray striped areas. Similarly, the nonempty intersections [Eq. (27) for $i = 1$], enforce that the escape lobes $\bar{\mathcal{E}}_0$ and $\mathcal{E}_0$ are pulled through the scattering region in a backward iteration. These escape lobes cut the remaining part of the scattering region into three disjoint stripes, thus enforcing a topological horseshoe. For an illustration, see Figs. 4, 5(c), and 5(d), where the nonempty intersections in Eq. (27) are marked by gray striped areas. Condition (26) can be checked numerically, using finite segments of the stable and unstable manifolds. We find that it is fulfilled for any numerically tested value $\kappa \gtrsim 10.5$.

*Complete horseshoe and uniform hyperbolicity?* Note that a topological horseshoe is not yet a sufficient condition for a complete horseshoe [81,82]. Proving a complete horseshoe might be achieved by checking the sector condition, described in Ref. [82], but was not attempted here. Note that a topological horseshoe further cannot guarantee the uniform hyperbolicity of the model system. The only numerical indication in this direction is obtained by constructing long but finite approximations to the stable and unstable manifolds. For any numerically tested value $\kappa \gtrsim 10.5$ we observe that these manifolds always intersect at finite angles (see Fig. 6 for the case $\kappa = 11$).

This finishes the construction of the model system. For the rest of the paper we will focus on the model system for $\kappa = 11$ where the topological horseshoe holds.

## IV. RESONANCE SPECTRA AND QUANTUM MAPS

In this section we derive quantum maps for kicked scattering systems and discuss the computation of their resonance spectra in terms of complex scaling and absorbing potentials. In particular, in Sec. IV D the method of complex scaling [53–57] as developed for time-periodic systems [58–62] is adapted to periodically kicked scattering systems. This results in the complex-scaled time-evolution operator (48), i.e., the complex-scaled quantum map from which resonance spectra can readily be computed (see Fig. 9). In Sec. IV E we further examine resonance spectra of heuristic model systems. To this end we adapt the method of complex absorbing potentials [49] to kicked scattering systems. This leads to an absorption-augmented time-evolution operator (54), which admits the form of a heuristic model. We show that this operator also allows for computing the resonance spectra of kicked scattering systems [see Fig. 10(b)], albeit only in the limit of weak absorption. On the other hand, we also show that strong absorption [Fig. 10(a)] and projective openings (Fig. 11), as commonly applied to heuristic models, fail to produce the resonance spectrum. An overview of the main ideas is given in Sec. IV A, while introductory remarks on Floquet theory and complex scaling are given in Secs. IV B and IV C, respectively.

### A. Computation of resonances: Overview

The main goal of Sec. IV is to numerically compute resonance spectra of periodically kicked scattering systems (1). Since this task can at times become quite technical, we give an outline of the key points and recommend Ref. [57] for a review.

#### 1. Resonances

Since periodically kicked scattering systems are unbound, they admit resonance solutions with eigenvalues in the lower half of the complex plane. Their real parts denote (quasi)energies, while their imaginary part describes the lifetimes of a resonance solution and may, for example, be associated with the width of a spectral line. Mathematically, a resonance is associated with the poles of the resolvent, analytically continued into the lower half of the complex plane. Thus, resonance states are to a scattering system as bound states are to a closed system, i.e., they allow for efficient basis expansions of wave packets, scattering cross sections, or the scattering matrix (see Ref. [57] for an overview).

#### 2. Challenges

In numerical computations of resonance spectra, we face several challenges which are unfamiliar in closed systems. (i) Resonance states are not square integrable. Even worse, they diverge at infinity. Hence, they cannot be computed by simple basis-state expansions. (ii) In contrast to closed systems, a scattering system also contains a continuous spectrum, associated with scattering solutions which neither diverge nor decrease in the asymptotic regions. In numerical computations, the remnants of this continuous spectrum must be separated from resonance eigenvalues. (iii) The time dependence of periodically kicked scattering systems poses an additional challenge.

#### 3. Floquet theory

The time-periodic structure of kicked scattering systems results in resonance solutions which are quasiperiodic in time [83,84]. The resonance eigenvalues, referred to as quasienergies, may be computed from either the so-called Floquet Hamiltonian or the stroboscopic time-evolution operator. Since the stroboscopic time-evolution operator is the quantum map, we here choose the second approach. Details are described in Sec. IV B.

#### 4. Complex scaling

In order to deal with the divergence of resonance states we adapt two standard methods to periodically kicked scattering systems, namely, complex scaling [53–57], as previously developed for time-periodic systems [58–62] and complex absorbing potentials, as previously discussed for time-independent systems [49].

The main idea of complex scaling [53–55] is to consider the system along a complex contour

$$\mathcal{C} : s \in \mathbb{R} \mapsto q \in \mathbb{C} \quad \text{with } q(s) := s \exp(i\theta), \tag{28}$$

determined by the scaling angle $\theta$. While this turns the Schrödinger equation into a non-Hermitian operator, it also changes the asymptotic behavior of resonance states. In particular, long-lived resonance states become square integrable, which makes their eigenvalues amenable to numerical computations using basis-state expansions. The method further rotates the continuous spectrum away from the real axis and thus allows for its effective separation from resonance eigenvalues. We emphasize that complex scaling is far more than just a numerical method to compute resonances. In particular, in the mathematical literature it is the method of choice for dealing with resonances; see, for example, Ref. [55] for time-independent systems, Refs. [85–87] for time-periodic systems, and Ref. [20] for open quantum maps. An introductory description of complex scaling for time-independent systems is given in Sec. IV C. The application of complex scaling to kicked scattering systems is discussed in Sec. IV D.

#### 5. Absorbing potentials

Adding suitable absorbing potentials to a scattering system represents an alternative method for computing resonance spectra [49]. The modified Hamiltonian generally supports neither resonance states nor a continuous spectrum. However, in the limit of weak absorption the point spectrum of the modified Hamiltonian mimics the resonance spectrum and the continuous spectrum of the original scattering system in a well understood manner [49]. Thus, resonance eigenvalues of a scattering system may be approximated by numerically computed point spectra of absorption-augmented Hamiltonians. The details of this method and its adaption to kicked scattering systems are discussed in Sec. IV E.

### B. Floquet theory and quantum maps

The Hamiltonian in Eq. (1) is time periodic and we have $\hat{H}(t) = \hat{H}(t+T)$ with $T = 1$ and $\omega = 2\pi/T$. Its solutions admit a quasiperiodic representation [83]

$$|\psi_\epsilon(t)\rangle = e^{-i\epsilon t/\hbar}|u_\epsilon(t)\rangle \quad \text{with } |u_\epsilon(t)\rangle = |u_\epsilon(t+1)\rangle \tag{29}$$

and $\epsilon$ being a quasienergy. The above decomposition is not unique. In particular, replacing $\epsilon$ by $\epsilon + n\omega\hbar$ and simultaneously multiplying $|u_\epsilon(t)\rangle$ by $\exp(in\omega t)$ yields identical solutions $|\psi_\epsilon(t)\rangle$ for any $n \in \mathbb{Z}$ [84]. In order to fix a unique representation of the solutions one can, for example, shift the real parts of the quasienergies to the first Floquet zone $\mathrm{Re}(\epsilon) \in [0,\omega\hbar)$.

In what follows we seek to determine the spectrum of quasienergies via the stroboscopic time-evolution operator $\hat{U}(t,t+T)$, henceforth referred to as $\hat{U}$. Applying this quantization of the classical map to a Floquet solution (29) and suppressing the index $t$ gives

$$\hat{U}|\psi_\epsilon\rangle = \exp\left(-i\frac{\epsilon}{\hbar}\right)|\psi_\epsilon\rangle. \tag{30}$$

Hence, the quasienergies are related to the eigenvalues $\lambda_\epsilon$ of the quantum map $\hat{U}$ as

$$\lambda_\epsilon := \exp\left(-i\frac{\epsilon}{\hbar}\right). \tag{31}$$

### C. Complex scaling for time-independent systems

In this section we briefly recall results of complex scaling of time-independent systems as obtained in Refs. [53–55] and reviewed in Refs. [56,57]. This section is intended as an introduction for nonexpert readers.

For the moment, consider a scattering system

$$\left[E + \frac{\hbar^2}{2}\frac{\partial^2}{\partial q^2} - V(q)\right]\phi_E(q) = 0, \tag{32}$$

with a time-independent potential satisfying Eq. (3). Since the system is unbound, its spectrum may contain resonance states, with eigenvalues in the lower half of the complex plane $\mathrm{Im}(E) < 0$.

However, resonance states are not square integrable. To illustrate this, consider the Schrödinger equation in the region $q \gg 1$ where $V(q)$ tends to zero. Here the solution takes the asymptotic form

$$\phi_E^\pm(q) \simeq \exp\left(\frac{ip^\pm(E)q}{\hbar}\right), \tag{33}$$

with momenta

$$p^\pm(E) = \pm\sqrt{|2E|}\exp\left(i\frac{\arg(E)}{2}\right). \tag{34}$$

Here the complex argument function $\arg(E)$ maps to values on the interval $(0,2\pi]$. This fixes the branch cut of the energy root along the positive real axis such that the following hold. (i) The first Riemann sheet $p^+$ gives square-integrable solutions. On this sheet the Hamiltonian is Hermitian and the corresponding spectrum must be real. (ii) The second Riemann sheet $p^-$ gives solutions which diverge as $q$ tends to infinity. Here one finds resonance solutions associated with eigenvalues in the lower half of the complex plane. (iii) The scattering solutions, which neither decay nor diverge as $q$ tends to infinity, are along the branch cuts which separate both sheets. They give the continuous spectrum along the positive real axis (see Fig. 7 for a sketch).

This illustrates that a resonance wave function cannot be square integrable. In the theory of complex scaling [53–55] this problem is dealt with by considering wave functions along a complex contour (28), resulting in the complex-scaled wave function

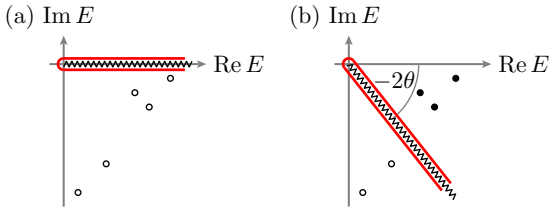


FIG. 7. Schematic spectra (a) before and (b) after complex scaling. Resonance eigenvalues are shown as circles. Open circles correspond to states that are not square integrable. Filled circles correspond to states that are square integrable. Continuous spectra are shown by lines. Branch cuts of the complex energy root (zigzag line) separate square-integrable from nonsquare-integrable solutions.

$$\phi_E^\theta(s) := \phi_E(q(s)) \tag{35}$$

and the complex-scaled Schrödinger equation

$$\left[E + \frac{e^{-i2\theta}\hbar^2}{2}\frac{\partial^2}{\partial s^2} - V(se^{i\theta})\right]\phi_E^\theta(s) = 0. \tag{36}$$

Here $\phi_E^\theta(s)$ is from a suitable subspace of square-integrable functions [53–55]. Note that we omit multiplying the wave function by a phase factor $\exp(i\theta/2)$, as it has no effect on the resulting spectra.

The utility of this transformation is that a part of the resonance states become square integrable. More precisely, if the potential $V(q)$ is dilation analytic [55], which implies that $V(q)$ has no singularity in the sector $\arg(q) \in [0,\theta]$ and further has the asymptotic behavior

$$\lim_{s\to\pm\infty} V(s\exp i\alpha) = 0 \quad \forall\alpha \in [0,\theta], \tag{37}$$

we have the following. (i) The point spectrum of the scaled Hamiltonian and the original Hamiltonian are identical [55]. In particular, eigenvalues corresponding to resonance states are invariant under variations of the scaling angle $\theta$ and those resonance states with eigenvalues in the sector $\arg(E) \in (-2\theta,0)$ become square integrable along the complex contour (28). (ii) The continuous spectrum of the scaled Hamiltonian is rotated into the lower half of the complex plane along the ray $\mathbb{R}_+\exp(-i2\theta)$.

In order to illustrate these properties, we consider the scaled equation in the region $s \gg 1$ where $V(s)$ tends to zero. Here the scaled form of the previously discussed asymptotic solutions reads

$$\phi_E^{\theta,\pm}(s) \simeq \exp\left(\frac{ip^\pm(E)s\exp(i\theta)}{\hbar}\right). \tag{38}$$

Note that these are the same solutions as in Eq. (33), now considered along the contour (28). This shows the following. (i) Solutions in the sector $\arg(E) \in (-2\theta,0)$ of the second Riemann sheet $p^-(E)$, as previously defined in Eq. (34), become square integrable when considered along the contour (28). It is these resonances that complex scaling makes accessible to numerical computations. (ii) The branch cut which separates the sheet of square-integrable solutions from the sheet of

solutions which diverge as $s$ tends to infinity is now located along the ray $\mathbb{R}_+ \exp(-i2\theta)$. This ray supports the scattering solutions of the scaled Hamiltonian which neither decay nor diverge as $s$ tends to infinity. It is along this ray that the scaled Hamiltonian has its continuous spectrum (see Fig. 7 for a sketch).

### D. Complex scaling for kicked scattering systems

In this section we adapt the method of complex scaling, as previously developed for periodically driven systems in Refs. [58–62,85–87], to periodically kicked scattering systems. To this end, we first derive the complex-scaled Floquet Hamiltonian, which is convenient for discussing the structure of the resulting spectra. We then derive an explicit expression for the complex-scaled time-evolution operator (48), i.e., the complex-scaled quantum map, and compute its spectrum (Fig. 9).

#### *1. Complex scaling for time-periodic Hamiltonians*

In order to apply complex scaling to time-periodic systems, we consider the Schrödinger equation (1) along the contour (28). This gives wave functions

$$\psi^\theta(s,t) := \psi(q(s),t) \tag{39}$$

and the complex-scaled Schrödinger equation

$$\left[ i\hbar\frac{\partial}{\partial t} + \frac{e^{-i2\theta}\hbar^2}{2}\frac{\partial^2}{\partial s^2} - V(se^{i\theta}) \sum_{n\in\mathbb{Z}} \delta(t-n) \right] \psi^\theta(s,t). \tag{40}$$

From Floquet theory, we infer the general form of a resonance state to admit the Fourier representation

$$\psi^\theta_\epsilon(s,t) = \sum_{\nu\in\mathbb{Z}} \phi^\theta_{\epsilon,\nu}(s) e^{-i(\epsilon+\hbar\omega\nu)t/\hbar}. \tag{41}$$

Inserting this representation of eigenstates into the scaled Schrödinger equation and integrating out the Fourier components results in a coupled-channel equation with channels $\mu \in \mathbb{Z}$. For kicked scattering systems the equation of the $\mu$th channel reads

$$\left[ \epsilon + \mu\hbar\omega + \frac{e^{-i2\theta}\hbar^2}{2}\frac{\partial^2}{\partial s^2} \right] \phi^\theta_{\epsilon,\mu}(s) = V(se^{i\theta}) \sum_{\nu\in\mathbb{Z}} \phi^\theta_{\epsilon,\nu}(s). \tag{42}$$

Note that this equation is usually derived [58–60,85–87] by first switching to the time-independent Floquet Hamiltonian and then applying complex scaling [54,55]. While we will not use it for numerical computations, it is convenient for discussing the structure of quasienergy spectra in time-periodic systems as done in the next section. Once again we emphasize the crucial point of complex scaling: By considering the system along a complex contour we change the asymptotic properties of resonance states. In particular, long-lived resonance states $\psi^\theta_\epsilon(s,t)$ and their Fourier components $\phi^\theta_{\epsilon,\nu}(s)$ become square integrable with respect to $s$.

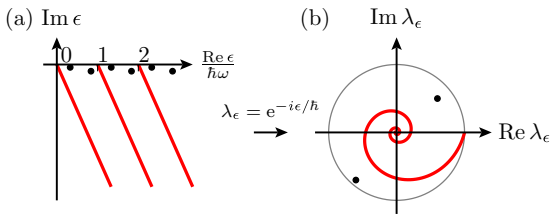


FIG. 8. Schematic spectra of time-periodic scattering systems, for the complex-scaled (a) Floquet Hamiltonian and (b) time-evolution operator. Resonance eigenvalues are shown as dots. Continuous spectra are shown as red lines. The gray line represents the unit circle.

#### *2. Structure of resonance spectra*

We now discuss the structure of the spectrum. To this end we consider the Floquet Hamiltonian (42) in the asymptotic region $s \gg 1$ where the potential tends to zero. This shows that the continuous spectrum of the $\mu$th channel is along the ray

$$\epsilon(b) = -\mu\hbar\omega + b\exp(-i2\theta) \quad \text{with } b \in \mathbb{R}_+, \tag{43}$$

where $-\mu\hbar\omega$ is the ionization threshold of the $\mu$th channel. On the other hand, the theory of complex scaling ensures that resonance eigenvalues in the lower half of the complex plane are invariant under variations of the scaling angle [53–55] (see Fig. 8 for a sketch and Ref. [60] for an example).

Note that the multichannel structure of the time-periodic system implies an additional feature. Namely, increasing the scaling angle may not only uncover resonances; in fact, a resonance eigenvalue may also be covered, if the continuous spectrum of another channel sweeps over them [88,89]. This phenomenon and the corresponding structure of resonance states are discussed in Appendix B.

The spectrum of the Floquet Hamiltonian (42) is periodic under shifts by integer multiples of $\omega\hbar$. This is because any solution $(\epsilon,\phi^\theta_{\epsilon,\mu}(s))$ gives rise to further solutions $(\epsilon',\varphi^\theta_{\epsilon',\mu'}(s)) = (\epsilon + n\omega\hbar,\phi^\theta_{\epsilon,\mu'+n}(s))$ with shifted eigenvalue. Note that any of these shifted solutions gives rise to the identical Floquet solution (41) such that the full spectral information is already stored in the first Floquet zone. Here we extend this zone into the complex domain along the rays of the continuous spectrum

$$\mathcal{F} := \{\epsilon \in \mathbb{C} : \epsilon = a + be^{-i2\theta}, a \in [0,\hbar\omega), b \in \mathbb{R}_+\}. \tag{44}$$

As discussed in Appendix B a resonance state is square integrable and thus amenable to numerical computations if the scaling angle $\theta$ is chosen such that the quasienergy $\epsilon$ associated with the resonances lowest outgoing channel is located in the Floquet zone $\epsilon \in \mathcal{F}$.

Rather than using the Floquet Hamiltonian (42) we will follow the ideas of Refs. [61,62] and compute the resonance spectrum via the eigenvalues of the stroboscopic time-evolution operator. As discussed in Sec. IV B, both eigenvalues are related by Eq. (31). This shows that both resonance eigenvalues and the continuous spectrum should localize within the unit circle. Furthermore, combining Eqs. (31) and (43) the continuous spectrum should localize along a spiral, given by

$$\lambda(b) = \exp[-ib\exp(-i2\theta)] \quad \text{with } b \in \mathbb{R}_+ \tag{45}$$

(see Fig. 8 for a sketch).

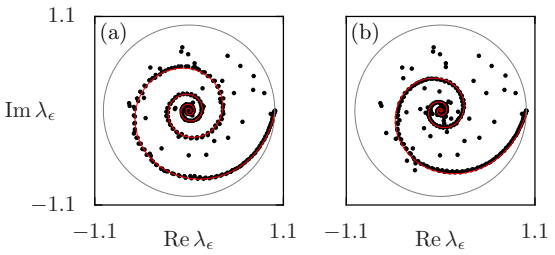


FIG. 9. Numerically determined eigenvalues (black dots) of the complex-scaled time-evolution operator (48) for scaling angles (a) $\theta = 0.05$ and (b) $\theta = 0.08$. The parameters of the model system are $\kappa = 11$ and $h_{\text{eff}} = 1/50$. The $\theta$-dependent continuous spectrum is along a spiral (red line). The gray line represents the unit circle.

#### 3. Complex-scaled time-evolution operator

We now derive the complex-scaled time-evolution operator, i.e., the quantum map from Eq. (40). Clearly, in between two kicks the potential term is irrelevant and the particle is subject to free motion in the complex-scaled Hamiltonian. This gives the propagator of a free particle in its complex-scaled form

$$\langle s'|\hat{U}^{\theta}_{VG}|s\rangle = \frac{\exp(i[\theta-\pi/4])}{(2\pi\hbar)^{1/2}}\exp\left(\frac{ie^{i2\theta}}{\hbar}\frac{(s-s')^2}{2}\right). \quad (46)$$

On the other hand, during the extremely short and intense pulse, the kinetic energy term of Eq. (40) is irrelevant and the wave function acquires a phase which is determined by the kicking potential

$$\langle s'|\hat{U}^{\theta}_{HK}|s\rangle = \delta(s-s')\exp\left(-\frac{i}{\hbar}V(se^{i\theta})\right). \quad (47)$$

Combining these operators, we obtain the complex-scaled version of the time-evolution operator (6) as

$$\langle s'|\hat{U}^{\theta}|s\rangle = \frac{\exp(i[\theta-\pi/4])}{(2\pi\hbar)^{1/2}}\exp\left(-\frac{i}{2\hbar}V(s'e^{i\theta})\right.$$
$$\left.+\frac{ie^{i2\theta}}{\hbar}\frac{(s-s')^2}{2}-\frac{i}{2\hbar}V(se^{i\theta})\right). \quad (48)$$

This is the complex-scaled quantum map. We emphasize that knowing the explicit form of the complex scaled time-evolution operator is an advantage of kicked scattering systems over general time-periodic systems [61,62].

#### 4. Numerical spectra

We now discuss the computation of the resonance spectrum from the complex-scaled time-evolution operator. The numerical computations are carried out by expanding the operator in Eq. (48) on a basis set of square-integrable functions and computing its eigenvalues. In particular, our implementation follows Refs. [90,91]. That is, we choose a finite-element representation which allows for representing square-integrable resonance wave functions with very high accuracy and thus allows for computing highly accurate resonance eigenvalues. Details are described in Appendix C. The results for the model system at kick strength $\kappa = 11$ and $h_{\text{eff}} = 1/50$ are illustrated in Fig. 9, for two values of the scaling angle $\theta$.

As expected from Eq. (45), the numerical remnants of the continuous states are localized along a spiral, marked by a red line in Fig. 9. Clearly, those states depend on the scaling angle $\theta$, giving two distinct spiral configurations in Figs. 9(a) and 9(b). On the other hand, we find stable $\theta$-independent eigenvalues away from the spiral which correspond to resonance states.

We now make a couple of remarks. (i) The resonance states, associated with eigenvalues which are sufficiently away from the continuous spectrum, are exponentially localized along the contour (28) (not shown). For this reason, their eigenvalues are extremely stable not only under variations of the scaling angle, but also under variations of other numerical parameters, such as the length of the grid. (ii) In contrast, the numerical eigenstates associated with the remnants of the continuous spectrum do not decay towards the edges of the numerical grid. For this reason their eigenvalues are affected by finite-size effects of the numerical computation. In particular, at large kick strength the numerical remnants of the continuous spectrum are not localized exactly along the spiral predicted by Eq. (45). For this reason the red lines in Fig. 9 originate from Eq. (45), where scaling angles have been enlarged over the theoretically expected value by factors of 1.5 [Fig. 9(a)] and 1.3 [Fig. 9(b)]. (iii) Note that numerically computed resonance states are along the contour $\mathcal{C}$. Backscaling such states to the real axis $q \in \mathbb{R}$ is numerically unstable. Therefore, the presented results cannot provide insight into the localization of resonance states in real phase space. This could be achieved using the method of exterior complex scaling [57] and remains a future task.

### E. Resonance spectra from absorbing potentials

The main purpose of this paper, namely, the computation of resonance spectra for periodically kicked scattering systems, was achieved in the preceding section. The main motivation for the rest of this paper is to make a connection to the approach termed heuristic models in the Introduction. Namely, we would like to discuss to what extent it is possible to obtain the resonance spectra of periodically kicked scattering systems, by adding absorption to its time-evolution operator.

This section will start with a short review of Ref. [49], in which it was proven that adding a complex absorbing potential

$$V_\eta(q) = -i\eta v(q) \quad (49)$$

to a time-independent Hamiltonian and letting the absorption strength $\eta \in \mathbb{R}_+$ tend to zero ($\eta \to 0$) allows for computing the resonance spectrum. We will then adapt the method of absorbing potentials to periodically kicked scattering systems in a rather heuristic manner, namely, by adding an absorbing potential to the kick. This will result in an absorption-augmented time-evolution operator (54), which takes exactly the form of heuristic model systems. We then demonstrate that the spectra of the absorption-augmented time-evolution operator indeed recover the resonance spectra of the model system in the limit of weak absorption ($\eta \ll 1$) (see Fig. 10). In contrast, we also show that the resonance spectra of the model system cannot be recovered if applying projective openings in the outgoing regions. Finally, we remark that the notion of absorbing potential, as used in this paper, is distinct from any sort of exterior complex scaling, which from time to time is also referred to as an absorbing potential in the literature.

#### 1. Time-independent systems

The computation of resonance spectra of time-independent Hamiltonian systems based on complex absorbing potentials (49) was established in Ref. [49]. The main idea of the method is quite different from complex scaling in the following sense: While complex scaling considers the same system along a different contour in coordinate space, the method of absorbing potentials adds a complex absorbing potential to the scattering system. As previously emphasized in Sec. IV A, this changes the properties of the system entirely. In particular, the absorption-augmented scattering system is usually closed and exhibits neither a continuous spectrum nor resonance states. However, in the limit of weak absorption $\eta \to 0$ the point spectrum of the modified system approximates the resonance eigenvalues of the original system in a well-controlled manner.

More specifically, the method of absorbing potentials [49] adds an absorbing potential (49) to the Schrödinger equation. As specified in Ref. [49], one may use a wide class of potentials $v(q)$ which fulfill certain properties. In particular, in the asymptotic regions we require the real part of $v(q)$ to tend to infinity. Here we assume $v(q)$, which fulfill the conditions spelled out in Ref. [49], with asymptotic forms of a monomial

$$v(q) \simeq |q|^n \quad \text{for } |q| \gg 1,\ n > 0. \tag{50}$$

In that case, the results of Ref. [49] state that, adding an absorbing potential (49) to a time-independent Hamiltonian (32) and considering the limit of weak absorption $\eta \to 0$, the spectra of the absorption-augmented Hamiltonians will converge onto the following shapes. (i) The remnants of the continuous spectrum (referred to as the spectral string in Ref. [49]) will arrange along the ray $\mathbb{R}_+ \exp(-i2\bar{\theta})$, with

$$\bar{\theta} = \frac{\pi}{2n+4}. \tag{51}$$

(ii) For each resonance solution of Eq. (32) with energy $E$ in the sector $\arg(E) \in (-2\bar{\theta},0)$, the family of absorption-augmented Hamiltonians gives a family of eigenvalues $E(\eta)$ which tends to the resonance eigenvalue $E$ of the scattering system as $\eta$ tends to zero, according to

$$\lim_{\eta\to 0} E(\eta) = E. \tag{52}$$

We now make a couple of remarks. (i) The structure of the spectrum and in particular the role of the angle $\bar{\theta}$ is reminiscent of complex scaling. (ii) In numerical computations the strength of the absorbing potential must be reduced successively while simultaneously monitoring the convergence of the corresponding spectra. (iii) The intuitive interpretation of the complex absorbing potential method is as follows. In order to compute the resonance spectrum, we add an absorbing potential which turns the asymptotic, exponentially diverging and outgoing parts of a resonance state into a square-integrable solution. However, by adding an absorbing potential, we introduce unphysical backreflections from the absorbing potential itself, which deteriorate the quality of the solution. In order to minimize this unphysical backreflection, we have to consider the limit of weak absorption $\eta \ll 1$ in which the quality of the solution improves.

#### 2. Absorption-augmented time-evolution operator

We now adapt the results of Ref. [49] to periodically kicked scattering systems in an *ad hoc* manner. That is, rather than adding the complex absorbing potential to the Schrödinger equation, we add it directly to the kicking potential

$$\left[ i\hbar\frac{\partial}{\partial t} + \frac{\hbar^2}{2}\frac{\partial^2}{\partial q^2} - [V(q) + V_\eta(q)]\sum_{n\in\mathbb{Z}}\delta(t-n)\right]\psi(q,t) = 0. \tag{53}$$

The motivation for doing so is twofold. (i) Grouping the complex absorbing potential with the kick potential allows for a straightforward computation of the corresponding time-evolution operator. (ii) Our physical intuition is that grouping the complex absorbing potential with the kick will do an equally good job in transforming the asymptotic parts of a resonance solution into square-integrable functions and thus allows for computing the resonance spectrum.

As in the preceding section, we will access the quasienergy spectrum of Eq. (53) via the corresponding time-evolution operator. This time-evolution operator is easily obtained by taking the time-evolution operator of the preceding section, Eq. (48), considering it for scaling angle $\theta = 0$, relabeling $s$ by the standard variable $q$, and replacing $V(q)$ by $V(q) - i\eta v(q)$. This gives the absorption-augmented time-evolution operator according to

$$\langle q'|\hat{U}^\eta|q\rangle = P^\eta(q')\frac{\exp(-i\pi/4)}{(2\pi\hbar)^{1/2}}\exp\left(-\frac{i}{2\hbar}V(q') + \frac{i}{\hbar}\frac{(q-q')^2}{2} - \frac{i}{2\hbar}V(q)\right)P^\eta(q). \tag{54}$$

Here the complex absorbing potential has been split from the standard kicking potential. This gives the absorption-augmented time-evolution operator as a composition of the standard unitary time-evolution operator of the kicked scattering system, multiplied with an absorption operator

$$P^\eta(q) = \exp\left(-\frac{\eta}{2\hbar}v(q)\right) \tag{55}$$

from its left and its right. Note that Eq. (54) takes the typical form of a system, termed the heuristic model in the Introduction.

We will now explore under what condition absorbing potentials allow for computing the resonance spectrum of a kicked scattering system. To this end, we consider the model system of this paper and compute the corresponding spectrum of Eq. (54) for weak and strong absorbing potentials as well as projective openings. This will show that only for weak absorbing potentials the resonance spectrum of Eq. (54) coincides with the result obtained from complex scaling.

#### 3. Weak absorbing potentials

In order to adapt the method of Ref. [49] and check it for the model system of this paper, we set $v(q)$ such that

$$v(q) = \left[M_n^\xi(q - q_{\text{abs}}) + M_n^\xi(-q - q_{\text{abs}})\right]. \tag{56}$$

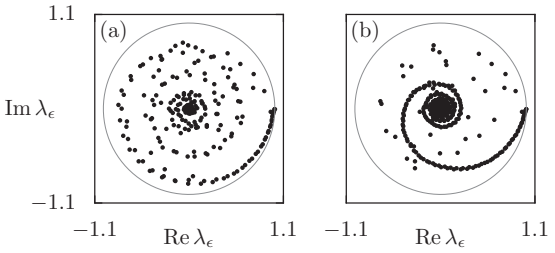


FIG. 10. Numerically determined eigenvalues (black dots) of the time-evolution operator (54) with (a) strong and (b) weak absorption, for $\kappa = 11$ and $h_{\text{eff}} = 1/50$. The parameters of the absorbing potential are $q_{\text{abs}} = 2.5$, monomial order $n = 3$, and width parameter $\xi = 0.1$. The absorption strength $\eta$ is determined by the length of the numerical grid $q_{\max}$ according to Eq. (58) as (a) $q_{\max} = 2.51$ (strong absorption) and (b) $q_{\max} = 5.0$ (weak absorption). The unit circle is marked by a gray line.

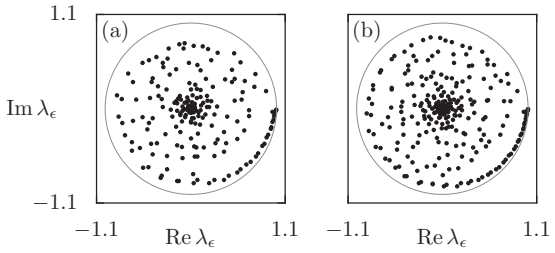


FIG. 11. Numerically determined eigenvalues (black dots) of the time-evolution operator with projective openings for $\kappa = 11$ and $h_{\text{eff}} = 1/50$. The projector removes probability for positions $|q| > q_{\text{abs}}$, where (a) $q_{\text{abs}} = 2.0$ and (b) $q_{\text{abs}} = 2.5$. The unit circle is marked by a gray line.

Here $M_n^\xi(x)$ is a smooth function which approaches a monomial when taking its smoothness parameter $\xi$ to zero as

$$\lim_{\xi\to 0} M_n^\xi(x) = \begin{cases} 0 & \text{if } x < 0 \\ x^n & \text{if } x \geqslant 0. \end{cases} \tag{57}$$

For details see Appendix C 7. This gives an absorbing potential which is close to zero for $q \in (-q_{\text{abs}}, q_{\text{abs}})$ such that the scattering region is unaffected by absorption.

In order to numerically determine the spectrum of $\hat{U}^\eta$ [Eq. (54)], we expand the corresponding modes. To this end we choose a finite-element representation on a grid with $q \in [-q_{\max}, q_{\max}]$ (see Appendix C for details).

In numerical computations we implement the limit of weak absorption ($\eta \ll 1$) by choosing the absorption strength as a function of the grid parameter $q_{\max}$,

$$\eta(q_{\max}) = -\frac{2\hbar}{v(q_{\max})} \ln(10^{-15}). \tag{58}$$

This choice ensures that the absorption operator, defined in Eq. (55), fulfills

$$P^\eta(q) < 10^{-15} \ \forall |q| > q_{\max} \tag{59}$$

such that any probability which is propagated beyond the grid edges by the unitary part in Eq. (54) will be reduced below machine precision. The expert reader might notice that this eliminates the error of backreflections from the grid edges within the numerical desired accuracy. We then minimize the backreflections from the absorbing potential itself. To this end we reduce the absorption strength $\eta$ successively by increasing the grid size $q_{\max}$ via Eq. (58). Simultaneously we monitor the convergence of the spectra.

The results are depicted in Fig. 10 where Fig. 10(a) shows a spectrum for which the absorption strength was large while Fig. 10(b) shows a spectrum for which the absorption strength was small. These results show the following. (i) The agreement between the spectrum in Fig. 10(b) with the spectra obtained from complex scaling (Fig. 9) is striking. (ii) We expect that the spiral structure in Fig. 10(b) corresponds to the remnants of the continuous spectrum. This expectation is supported by the structural analogy between spectra of time-independent systems obtained from complex scaling, on the one hand, and absorbing potentials, on the other hand. (iii) We further observe that the eigenvalues away from the spiral in Fig. 10(b) are localized in exactly the same positions as the resonance spectrum obtained from complex scaling in Fig. 9. These eigenvalues should represent the resonance spectrum. (iv) On the other hand, the spectrum in Fig. 10(a), as obtained for strong absorption, has little resemblance to the results obtained from complex scaling (Fig. 9). In particular, the continuous spectrum blows up and the separation between resonance spectra and continuous spectra is lost. We expect that this is due to unphysical reflections from the absorption operator which deteriorate the quality of the solution. In conclusion, we believe that the resonance spectrum of periodically kicked scattering systems can only be obtained from the absorption-augmented time-evolution operators in the limit of weak absorption.

Finally, we speculate on the generality of the method. While the results of this section have been obtained for one specific model system, we are positive that the method of weak absorbing potentials should allow for computing resonance spectra of any periodically kicked scattering system. We believe so, since the absorbing potential chosen here is nonzero only in the outgoing regions. Here its only task is to tweak the exponentially diverging tales of the resonance wave functions into square-integrable functions. However, this structure is universally the same for any kicked scattering system. Nonetheless, putting the method on an equally solid mathematical footing as in the case of time-independent systems [49] or in the case of complex scaling, as discussed in the preceding section, remains a future task.

#### *4. Projective opening*

Finally, we consider the case of projective openings, as commonly used for heuristic model systems, and show that they do not reproduce the resonance spectrum of a kicked scattering system. To this end we consider an absorbing potential which is zero for $q \in (-q_{\text{abs}}, q_{\text{abs}})$ and infinitely large outside of this interval. This turns the absorption operator (55) into a projector

$$P^\eta(q) := \begin{cases} 1 & \text{if } q \in (-q_{\text{abs}}, q_{\text{abs}}) \\ 0 & \text{if } q \notin (-q_{\text{abs}}, q_{\text{abs}}). \end{cases} \tag{60}$$

Here we choose sufficiently large $q_{\text{abs}}$ such that the scattering region and the trapped set in particular are unaffected. Based on this setting, we consider the absorption-augmented time-

evolution operator (54) and compute its spectrum numerically (see Appendix C for details of the numerical computation). The result is depicted in Fig. 11 for $q_{\mathrm{abs}} = 2.0, 2.5$.

These results show the following. (i) Spectra obtained with projective openings have little resemblance to the resonance spectrum obtained from complex scaling (see Fig. 9) or weak absorbing potentials [see Fig. 10(b)]. (ii) Similar to the case of strong absorption [Fig. 10(a)], we observe that the continuous spectrum blows up. In particular, the clear separation of the continuous spectrum and the resonance spectrum is lost. We speculate that the origin of this problem is again due to unphysical backreflections into the scattering region which originate from the nonanalytic corners of the absorbing potential. We conclude that resonance spectra of kicked scattering systems are not computable by virtue of projective openings. (iii) Our results also have important implications for numerical tests of the fractal Weyl law, based on heuristic model systems. Namely, if we were to follow the standard recipe of heuristic models and construct an open quantum map for the model system of this paper we would apply projective openings in the outgoing region far away from the trapped set. However, our results show that the eigenvalues of this system have no relation to the true resonance eigenvalues of the kicked scattering system, as obtained from complex scaling or sufficiently weak absorbing potentials. Hence, counting long-lived eigenvalues of heuristic model systems may not be a reasonable test for the fractal Weyl conjecture.

## V. SUMMARY AND DISCUSSION

In this paper we had two main objectives.

(i) We introduced a class of open quantum maps, induced by periodically kicked scattering systems. For this class of open quantum maps we showed how to compute the resonance spectra in terms of theoretically grounded methods by making use of either complex scaling or weak absorbing potentials.

(ii) On the other hand, we demonstrated that prevalent implementations of open quantum maps, called heuristic models throughout this paper, based on strong absorptive or even projective openings suffer from a number of deficiencies, i.e., they cannot reproduce the resonance spectra of periodically kicked scattering systems, they cannot provide a clear separation of resonance eigenvalues from the continuous spectrum, and they suffer from diffraction effects due to strong absorptive potentials.

In order to obtain our results, we employed the following methodology. Our starting point was the class of periodically kicked scattering systems, as defined in Sec. II. For this class of systems, we introduced a representative example in Sec. III. By discussing its phase-space structures, we argued that kicked scattering systems are excellent toy models of ionization and dissociation. Furthermore, we established the utility of kicked scattering systems for explorations of quantum-chaotic scattering systems, by showing that our model system exhibits a topological horseshoe at large kick strength.

We then turned our attention to quantum aspects of kicked scattering systems in Sec. IV. In particular, we applied the method of complex scaling [53–57] as previously developed for time-periodic systems [58–62] to kicked scattering systems. This resulted in a complex-scaled time-evolution operator (48), i.e., the complex-scaled quantum map, from which resonance spectra of kicked scattering systems could readily be computed [see Figs. 9 and 1(a)].

Furthermore, we examined the relation between the complex-scaled quantum map and heuristic models. To this end, we adapted the method of absorbing potentials [49] to periodically kicked scattering systems in Sec. IV E. This resulted in an absorption-augmented time-evolution operator (54), which takes the form of heuristic models. We showed that this operator also allows for computing resonance spectra of kicked scattering systems, albeit only in the limit of sufficiently weak absorption [see Fig. 10(b) or 1(b)]. On the other hand, we also showed that neither strong absorption [Fig. 10(a) or 1(c)] nor projective openings [Fig. 11 or 1(d)], as commonly used for heuristic models, allow for computing the resonance spectra of kicked scattering systems.

### A. Conclusion

Our results show that the strategy of heuristic model systems, i.e., combining an arbitrary unitary time-evolution operator with an arbitrary absorption operator, such as a projector, does not produce the correct resonance spectrum of kicked scattering systems and cannot in general be expected to faithfully model the resonance spectrum of a scattering system. Moreover, our results hint at two conceptual deficiencies in heuristic models:

(i) the inability to separate true resonance eigenvalues from the continuous spectrum and

(ii) the presence of diffraction effects due to strong absorptive or projective openings.

The inability to separate true resonance eigenvalues from the continuous spectrum is best illustrated in Fig. 1, which depicts the spectrum of the model system for various implementations. In particular, Fig. 1(a) shows the spectrum obtained from complex scaling. Here a clear separation of resonance eigenvalues, on the one hand, and the continuous spectrum (located along a spiral), on the other hand, is found. This separation of eigenvalues can also be observed for sufficiently weak absorbing potentials [Fig. 1(b)]. On the other hand, upon increasing the absorption strength [to smoothly interpolate between Figs. 1(b) and 1(c)] we observe a blowup of the continuous spectrum. As a result, resonance eigenvalues and the continuous spectrum are indistinguishably intermingled in Fig. 1(c). A similar situation is observed for projective openings in Fig. 1(d). We emphasize that the blowup of the continuous spectrum appears, even though the openings of the heuristic model do not affect the classical trapped set. It is further worth noting that the blowup of the continuous spectrum affects shorter-lived resonances in particular, e.g., those associated with chaotic dynamics.

We further claim that our results hint at the presence of nonclassical diffraction effects in heuristic implementations of open quantum maps. In order to understand our claim, we remind the reader that resonance eigenvalues are semiclassically determined by the periodic orbits within the classical trapped set (see, e.g., Ref. [9]). However, while the classical trapped set is identical for all implementations of our model system, the resonance spectra, as obtained from complex scaling and weak absorbing potentials [see Figs. 1(a)

and 1(b)], differ greatly from the spectra, as obtained with strong absorptive and projective openings [see Figs. 1(c) and 1(d)]. We conjecture that this discrepancy originates from the nonclassical diffraction effect in heuristic models, presumably due to rapidly varying or nonanalytic parts in the strong absorptive or projective openings, respectively.

### B. Discussion

We now discuss several aspects of our result.

#### 1. The effect of absorption

Proponents of heuristic model systems often argue that absorbing potentials should not affect the resonance spectrum as long as the absorption does not affect the classical trapped set. Our results clearly indicate that this argument is wrong in two ways. First, in a true scattering system absorption does affect the tails of the resonance states in the asymptotic regions. In that, it directly affects resonance eigenvalues. Second, absorption exhibits a profound impact on the scattering states which support the continuous spectrum. Both effects heavily degrade the quality of numerically computed spectra if absorption is too strong. This fact is well established in the quantum chemistry community, where either complex scaling [57] or weak absorbing potentials [49] are the established ways to compute resonance spectra. In this paper we merely repeat this result by adapting it to quantum maps originating from kicked scattering systems.

#### 2. Advantages of kicked scattering systems

Quantum maps derived from kicked scattering systems hold several advantages over heuristic model systems. In fact, kicked scattering systems originate from a well-defined scattering system. This allows for discussing their resonance spectra in a mathematically rigorous manner. In particular, the overall non-Hermiticity and the corresponding subunitarity of the resulting quantum map clearly originate, as they should, from the outgoing boundary condition of the scattering system at infinity. Furthermore, as long as the kicking potential is analytic, kicked scattering systems should be free from distracting diffraction effects. This is a considerable simplification for investigations of quantum-to-classical correspondence.

#### 3. Heuristic models

Our results clearly demonstrate that heuristic models suffer from serious conceptual deficiencies which question the credibility of their resonance spectra. In spite of this result, we do not wish to imply that heuristic models should altogether be abandoned. In fact, heuristic models are by far the simplest toy models. Thus, they represent a numerically inexpensive way for testing and shaping semiclassical hypothesis in scattering systems. Furthermore, they might well capture certain aspects of particular scattering systems, such as dielectric cavities [32,38], in a reasonable manner. Nonetheless, in view of our results we do believe that any result derived from heuristic models must certainly be corroborated by cross validation in more complete systems, where resonances are mathematically well defined.

#### 4. More complete model systems

As compared to heuristic models, the benefits of a kicked scattering system come at the price of a slightly increased effort in their numerical treatment. For this reason, one might wonder if it is worth bothering with kicked scattering systems at all. In particular, a wealth of more realistic model systems such as periodically driven systems [57,60–62,92], two-dimensional potential systems [93,94], three-disk scatterers [3], or atomic systems [10,95–99] are available and have widely been used for exploring ionizing scattering systems in the past. As always, whether to pick a toy model or a more realistic system is a matter of taste and should of course depend on the particular question at hand. Nonetheless, we do believe that there are several advantages in using kicked scattering systems. For example, the fact that both the classical and the quantum time evolution are known in an analytically closed form facilitates numerical computations, both classically and quantum mechanically. In particular, discussing small wavelength limits with effective Planck constants as small as $h_{\mathrm{eff}} = 1/100$ is still possible on a desktop PC. Moreover, the analytically closed form of the classical dynamics may ultimately allow for proving the uniform hyperbolicity of our model system in the limit of large kick strength.

#### 5. Fractal Weyl law

Recent years have witnessed a wealth of publications which make use of heuristic model systems, such as the open baker's map or the open standard map, in order to investigate the fractal Weyl conjecture [14–19,29–35,37–39]. In quantum maps, this conjecture states that the number of long-lived resonance states should grow as a power law whose exponent is related to the fractal dimension of the classical repeller [15]. In view of our results, we would like to express serious doubt as to whether this conjecture can be examined in heuristic model systems. As we show, applying the methodology of heuristic models to kicked scattering systems leads to numerically computed spectra in which true resonance eigenvalues and remnants of the continuous spectrum are intermingled in an indistinguishable manner. We see no reason why heuristic models, such as the open baker's map and the open standard map, would not suffer from similar deficiencies. We further believe that using heuristic models for investigations of spectral gaps [16], supersharp resonances [36], or the localization of resonances on the classical repeller [18,19] should similarly suffer from the inability to distinguish true resonance eigenvalues from remnants of the continuous spectrum.

At this point we wish to emphasize that our criticism is exclusively focused on the use of heuristic models for explorations of the fractal Weyl conjecture. On the other hand, there should be nothing wrong with the fractal Weyl conjecture itself. In fact, the fractal Weyl conjecture has been investigated in more complete physical settings [12,13,94]. On the other hand, the more mathematical literature on fractal Weyl conjectures does not require the use of concrete model systems at all. Instead, it proceeds in the abstract setting of the quantization of an open flow [15], which should not be hampered by any details of a practical implementation.

Finally, it is worth mentioning that the mathematical literature on fractal Weyl conjectures requires scattering systems

whose dynamics along the trapped set is uniformly hyperbolic. If our claim on diffraction is true, then two of the most prominent models of chaotic scattering, namely, the open baker's map and the three-disk scatterer, do exhibit diffraction effects. In our opinion this makes it worth investigating what role diffraction plays for the formation of the fractal Weyl law. On the other hand, it is worth searching for cleaner model systems which are uniformly hyperbolic but do not exhibit any diffraction. In our opinion, the model system of this paper is a good candidate for becoming a representative for this class of systems.

#### *6. Quantum map literature*

Finally, we specify the relation of our results to existing notions of quantum maps in the literature. Presumably dating back to Ref. [21], open quantum maps have been introduced in an *ad hoc* manner by combining a unitary operator of the kicked rotator with a projection operator at its boundaries. Until today, this remains the archetype of heuristic models. This approach became very popular and found many imitators over the years [14–19,22–41]. It is this type of model system which our paper criticizes and for which our paper wishes to present an alternative.

On the other hand, in more recent years the mathematical literature developed a much wider definition of open quantum maps [15,20,42]. According to this definition, open quantum maps quantize the flow of the scattering system along its trapped set. Such quantum maps represent a reduction of the scattering system to a subunitary operator which holds the essential information on its resonance states. While this definition is extremely powerful, it has so far only been used as an abstract framework, which allows for deriving fractal Weyl lower and upper bounds [15]. In our opinion, the open quantum maps of kicked scattering systems we present in this paper are examples of this mathematical class of open quantum maps, albeit not yet reduced to a finite-dimensional matrix.

Finally, we find it worth mentioning that the quantum map discussed in this paper is not only an open quantum map in the sense of Ref. [20]. It also is a pure quantum map in the sense of Refs. [73,74], which contains resonances due to its outgoing boundary conditions at infinity.

### C. Future directions

The model system proposed in this paper is an excellent model of ionization and should be immediately useful for future investigations of dynamical tunneling in systems with a mixed phase space as well as further investigations of the fractal Weyl law. For the latter, it would be useful if the uniform hyperbolicity of the proposed model system could be proven. In contrast to the three-disk scatterer and the open baker's map, this would result in a uniformly hyperbolic model system which is not affected by diffraction. Furthermore, a proof of uniform hyperbolicity would also be a firm basis for more detailed investigations of the model systems classical dynamics, e.g., in terms of Lyapunov exponents, escape rates, entropies, and fractal dimensions [1,100].

We further believe that the model system is a suitable candidate for investigating the localization of resonance states on classical invariant sets and their implications for the fractal Weyl law in more detail. In particular, the results of Refs. [14,33] are entirely based on the existence of a leak. The complement of its preimages down to the Ehrenfest time is used to specify the support of long-lived resonances. While such a leak might exist in dielectric cavities or quantum dots with leads, it certainly does not exist in ionizing scattering systems, such as helium. In such an ionizing scattering system the localization of resonance states on a fractal repeller must be understood with a different methodology. Our model system should be ideal for addressing this question. To this end, it is crucial to make exterior complex scaling available for kicked scattering systems, which remains a future task.

Ultimately, it would be desirable to reduce the open quantum maps of kicked scattering systems to a finite-dimensional subunitary operator from which the continuous spectrum has been removed. This would drastically facilitate numerical computations. To this end, it seems appealing to implement the reduction procedures of Ref. [20], which are based on the use of exterior complex scaling combined with the use of a conjugating function. Alternatively, one might also try to pursue that goal by putting the ideas of Ref. [34] to a test in a kicked scattering system. To that end one needs to project the time-evolution operator of a kicked system onto a finite-dimensional basis which is supported by the periodic orbits within the classical trapped set.

Finally, an interesting direction of future research concerns the scattering matrix of kicked scattering systems. In particular, we wonder to what degree the structure of a periodically kicked scattering system may allow for explicitly evaluating several formulas, described in Refs. [57,92]. This would be useful for providing an outside view on open quantum maps and could lead to further interesting results.

## ACKNOWLEDGMENTS

We gratefully acknowledge fruitful discussions with Eduardo G. Altmann, Arnd Bäcker, Stephen Creagh, Carl Dettmann, Italo Guarneri, Yasutaka Hanada, Takahisa Harayama, Jon Keating, Roland Ketzmerick, Martin Körber, Tamiki Komatsuzaki, Jizhou Li, Domenico Lippolis, Stéphane Nonnenmacher, Stefan Rotter, Yuzuru Sato, Sulimon Sattari, Susumu Shinohara, Henning Schomerus, Martin Sieber, Atsushi Tanaka, Gregor Tannor, Hiroshi Teramoto, Mikito Toda, and Stephen Wiggins. N.M. acknowledges financial support from Deutsche Forschungsgemeinschaft via Grant No. ME 4587/1-1.

## APPENDIX A: OUTGOING AND INCOMING REGION

In this section we show that a system with kicking potential as defined in Eqs. (7)–(11) gives rise to incoming and outgoing regions, as defined in Eqs. (12)–(15). We start by showing that an outgoing region $\mathcal{O}^+$ is ensured, in general, if

$$V'(q) < 0 \quad \forall q > x_{\mathrm{f}}. \tag{A1}$$

To demonstrate this claim we exploit the condition (A1) in Eq. (5a) to show that for all $(q_n, p_n) \in \mathcal{O}^+$, i.e., $\forall (q_n, p_n)$ such that $q_n > x_{\mathrm{f}}$ and $p_n > 0$, we have

$$q_{n+1} > q_n + p_n > q_n > x_{\mathrm{f}}, \tag{A2}$$

i.e., for points in $\mathcal{O}^+$ the position grows in one step of the iteration. Further, exploiting Eqs. (A1) and (A2) in Eq. (5b) shows that for all $(q_n, p_n) \in \mathcal{O}^+$ we have

$$p_{n+1} > p_n > 0, \tag{A3}$$

i.e., for points in $\mathcal{O}^+$ the momentum also grows in one step of the iteration. This means that for trajectories which enter $\mathcal{O}^+$ the position and momentum are monotonically increasing such that trajectories which enter $\mathcal{O}^+$ remain in $\mathcal{O}^+$. Furthermore, the above equations imply that if $(q_n, p_n) \in \mathcal{O}^+$, we have that future positions $q_m$ with $m > n$ grow at least as

$$q_{m+n} > q_n + (m-n)p_n, \tag{A4}$$

which shows that any trajectory entering the region $\mathcal{O}^+$ will escape to infinity as

$$\lim_{m\to\infty} q_m \to \infty. \tag{A5}$$

Note that for the model system in this paper the related properties for the regions $\mathcal{O}^-$, $\mathcal{I}^+$, and $\mathcal{I}^-$ follow due to parity and time-reversal symmetry.

We now show that condition (A1) holds for the model system of this paper. To this end we compute the derivative of the kicking potential (7) whose parts are defined in Eqs. (8) and (9) using the perturbation strength as defined in Eq. (10). The resulting derivative is

$$V'(q) = \kappa \exp(-8q^2) f(q), \tag{A6}$$

with

$$f(q) = q - x_\mathrm{f} \frac{\exp(16x_\mathrm{b}[q - x_\mathrm{f}]) - \exp(-16x_\mathrm{b}[q + x_\mathrm{f}])}{1 - \exp(-32x_\mathrm{f}x_\mathrm{b})}. \tag{A7}$$

Throughout this paper we choose $\kappa > 0$, which implies that $\kappa \exp(-8q^2) > 0$. Under this condition, showing that condition (A1) holds is equivalent to showing that

$$f(q) < 0 \quad \forall q > x_\mathrm{f}. \tag{A8}$$

We show that condition (A8) holds from the fact that $f(x_\mathrm{f}) = 0$ while $f(x)$ is strictly monotonically decreasing for $q \geqslant x_\mathrm{f}$. The latter can be shown from the derivative

$$f'(q) = 1 - 16x_\mathrm{b}x_\mathrm{f} \frac{\exp(16x_\mathrm{b}[q - x_\mathrm{f}]) + \exp(-16x_\mathrm{b}[q + x_\mathrm{f}])}{1 - \exp(-32x_\mathrm{f}x_\mathrm{b})} \tag{A9}$$

being strictly negative

$$f'(q) < 0 \quad \forall q \geqslant x_\mathrm{f}. \tag{A10}$$

The last condition is ensured by Eq. (11) and the fact that $q \geqslant x_\mathrm{f}$ implies that $\exp(16x_\mathrm{b}[q - x_\mathrm{f}]) \geqslant 1$, $\exp(-16x_\mathrm{b}[q + x_\mathrm{f}]) > 0$, and $[1 - \exp(-32x_\mathrm{f}x_\mathrm{b})]^{-1} > 1$.

## APPENDIX B: STRUCTURE OF RESONANCE STATES

In this Appendix we discuss the asymptotic structure of resonance states in Floquet scattering systems. We further discuss its relation to the phenomenon of covering and uncovering of resonances by crossings of the continuous spectrum.

We start by discussing the asymptotic structure of Floquet solutions for $\theta = 0$. To this end we take Eq. (41), insert it into the Schrödinger equation (1), and consider the asymptotic regions $q \gg 1$, where the potential vanishes. This gives

$$(\epsilon + \mu\hbar\omega)\phi_{\epsilon,\mu}(q) = -\frac{\hbar^2}{2}\frac{\partial^2}{\partial q^2}\phi_{\epsilon,\mu}(q). \tag{B1}$$

This shows that each component $\phi_{\epsilon,\mu}(q)$ is associated with an asymptotic energy $\epsilon + \mu\hbar\omega$. Its asymptotic form is a linear combination of solutions

$$\phi^{\pm}_{\epsilon,\mu}(q) \simeq \exp[ip^{\pm}(\epsilon + \mu\hbar\omega)q/\hbar], \tag{B2}$$

with momenta

$$p^{\pm}(\epsilon + \mu\hbar\omega) = \pm\sqrt{|2(\epsilon + \mu\hbar\omega)|}\exp\left(i\frac{\arg(\epsilon + \mu\hbar\omega)}{2}\right).$$

Here we fix the branch cut of the energy root along the positive real axis, i.e., the complex argument function $\arg(\cdot)$ maps to values on the interval $(0, 2\pi]$.

Associated with scattering solutions which have quasienergies within the first Floquet zone along the real axis $\epsilon \in [0, \hbar\omega)$, we introduce the following classification. (i) Energies with $\mu \geqslant 0$ correspond to open propagating channels, with $p^-$ an outgoing and $p^+$ an incoming solution. (ii) Solutions with $\mu < 0$ correspond to closed channels, with $p^+$ an exponentially decreasing evanescent and $p^-$ an exponentially increasing solution. In what follows we keep the terminology, even if $\epsilon$ is in the lower half of the complex plane.

A general scattering solution of a Floquet system consists of both incoming and outgoing solutions in the open channels and possibly evanescent components in the closed channels. If a solution is found which is purely outgoing in the open channels, we speak of a resonance solution, which admits the asymptotic form

$$\phi_{\epsilon,\mu}(q) \simeq \begin{cases} \exp[ip^-(\epsilon + \mu\hbar\omega)q/\hbar], & \mu \geqslant 0 \\ \exp[ip^+(\epsilon + \mu\hbar\omega)q/\hbar], & \mu < 0. \end{cases} \tag{B3}$$

A resonance state generally does not exist for real quasienergies but exhibits $\epsilon$ in the lower half of the complex plane. For this reason the outgoing solutions in the open channels diverge at infinity such that a resonance state is not square integrable and thus cannot be computed with a simple basis-state expansion of the Floquet solution (41).

Upon complex scaling, the asymptotic form of the components of the Floquet resonance solution becomes

$$\phi^{\theta}_{\epsilon,\mu}(s) \simeq \begin{cases} \exp[ip^-(\epsilon + \mu\hbar\omega)s\exp(i\theta)/\hbar], & \mu \geqslant 0 \\ \exp[ip^+(\epsilon + \mu\hbar\omega)s\exp(i\theta)/\hbar], & \mu < 0. \end{cases} \tag{B4}$$

In order to have a square-integrable solution (41), one requires every component to be square integrable. For this to be fulfilled, we require two conditions. (i) The scaling angle $\theta$ should be large enough such that all open channels become localized. This is fulfilled if $\arg(\epsilon) \in (-2\theta, 0)$. (ii) The scaling angle $\theta$ should be small enough such that all closed channels remain localized. This is fulfilled if $\arg(\epsilon - \hbar\omega) \in (-\pi, -2\theta)$.

Conversely, if condition (i) is violated, then there are still open channels which are not yet square integrable. If condition (ii) is violated, then there are closed channels which are no longer square integrable. Thus, we effectively have a branch cut along the line $\exp(-i2\theta)\mathbb{R}_+$, which separates square-integrable solutions from diverging solutions, on both the first and the second Riemann sheet (see Fig. 12 for a sketch).

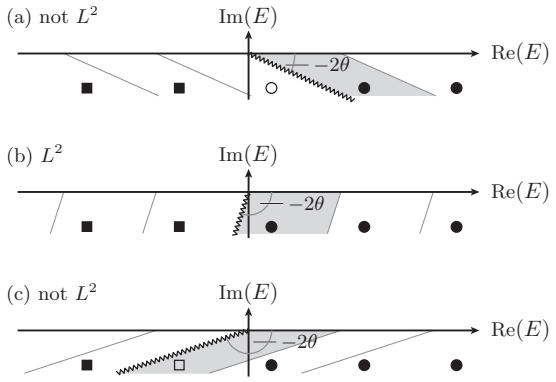


FIG. 12. Square integrability of a resonance state in a Floquet system for increasing scaling angle $\theta$. The asymptotic energies of its components are shown by squares and circles. Circles denote open channels with outgoing solutions on the second Riemann sheet. Squares denote closed channels with localized solutions on the first Riemann sheet. Filled symbols denote square-integrable components. Open symbols denote components that are not square integrable. The branch cut (zigzag line) separates square-integrable components from components that are not square integrable, on both the first and the second Riemann sheet. Gray lines mark the Floquet zone and the first zone is mark by a gray shaded region.

Note that conditions (i) and (ii) are equivalent to saying that a resonance state has square-integrable components if the quasienergy $\epsilon$ associated with the lowest open channel is in the first Floquet zone (44). This explains why upon increasing the scaling angle a resonance in a Floquet system can be both uncovered and later covered again.

## APPENDIX C: NUMERICAL METHODS

In this Appendix we describe the numerical computation of eigenvalues for operators in Eqs. (48) and (54). The scheme is based on a finite-element representation of the wave function and follows the ideas of Refs. [90,91]. The benefit of using a finite-element scheme is to achieve numerically determined eigenvalues with high accuracy. We describe the representation of the wave function in Appendix C 1 and the representation of operators in Appendix C 2. Details specific to complex scaling, projective openings, and weak absorbing potentials are discussed in Appendixes C 5–C 7, respectively.

### 1. Representation of wave functions

We now introduce the finite-element representation of wave functions $\psi(x)$. Here $x$ may refer to either the coordinate $s$ of Sec. IV D or $q$ of Sec. IV E.

We start by introducing a grid in coordinate space using grid points

$$x_0 < x_1 < \cdots < x_{N-1} \quad \text{with } x_l \in \mathbb{R}. \tag{C1}$$

We set the grid size as

$$x_{\max} := x_{N-1} = -x_0. \tag{C2}$$

We define the $l$th cell of the discretization as

$$x \in [x_l, x_{l+1}]. \tag{C3}$$

#### a. Basis functions in the lth cell

We now introduce basis functions, which are nonzero only in the $l$th cell. We start from Legendre polynomials on the interval $[-1,1]$, as defined by the recursion

$$(n+1)\bar{P}_{n+1}(y) = (2n+1)y\bar{P}_n(y) - n\bar{P}_{n-1}(y), \tag{C4}$$

with $\bar{P}_0 = 1$ and $\bar{P}_1 = y$. The polynomials fulfill $P_n(1) = 1$, a symmetry property $P_n(y) = (-1)^n P_n(-x)$, and an orthogonality relation

$$\int_{-1}^{1} P_n(y)P_m(y)dy = \frac{2}{2n+1}\delta_{m,n}, \tag{C5}$$

where $\delta_{m,n}$ is the Kronecker delta function. From these polynomials we introduce a set of polynomials

$$\bar{\chi}_n(y) := \begin{cases} \frac{1}{2}\bar{P}_0(y) - \frac{1}{2}\bar{P}_1(y) & \text{if } n = 0 \\ \bar{P}_{n+1}(y) - \bar{P}_{\mathrm{mod2}(n+1)}(y) & \text{if } n = 1,\ldots,m_{\max}-1 \\ \frac{1}{2}\bar{P}_0(y) + \frac{1}{2}\bar{P}_1(y) & \text{if } n = m_{\max}, \end{cases} \tag{C6}$$

which vanish at the edges of the interval $[-1,1]$. The only exceptions are $\bar{\chi}_0(-1) = \bar{\chi}_{m_{\max}}(1) = 1$.

We scale these polynomials to the $l$th cell using the linear transformation

$$y^{(l)}(x) := \frac{2x - (x_l + x_{l+1})}{x_{l+1} - x_l}, \tag{C7}$$

resulting in the scaled basis functions on the $l$th cell

$$\chi_n^{(l)}(x) := \bar{\chi}_n(y^{(l)}(x)). \tag{C8}$$

We emphasize that $\chi_n^{(l)}$ is defined to be zero outside the $l$th cell. Note that for all cells $l = 0,\ldots,N-1$ we have

$$\chi_n^{(l)}(x_l) = \begin{cases} 1 & \text{if } n = 0 \\ 0 & \text{otherwise,} \end{cases} \tag{C9a}$$

$$\chi_n^{(l)}(x_{l+1}) = \begin{cases} 1 & \text{if } n = m_{\max} \\ 0 & \text{otherwise.} \end{cases} \tag{C9b}$$

#### b. Wave function

We can now write the wave function along the grid as

$$\psi(x) = \sum_{l=0}^{N-1}\sum_{n=0}^{m_{\max}} c_n^{(l)}\chi_n^{(l)}(x). \tag{C10}$$

In order to ensure the continuity of this wave function, we exploit the property (C9) and impose an additional constraint

$$c_{m_{\max}}^{(l)} = c_0^{(l+1)} \quad \forall l = 0,\ldots,N-2. \tag{C11}$$

In order to handle dependent and independent coefficients, we arrange the dependent coefficients into a vector

$$\begin{pmatrix} c_0 \\ c_1 \\ \vdots \\ \vdots \\ \vdots \\ c_\alpha \\ \vdots \\ \vdots \\ \vdots \\ c_{\alpha_{\max}} \end{pmatrix} = \begin{pmatrix} c_0^{(0)} \\ \vdots \\ c_{m_{\max}}^{(0)} \\ c_0^{(1)} \\ \vdots \\ c_{m_{\max}}^{(1)} \\ \vdots \\ c_0^{(N-1)} \\ \vdots \\ c_{m_{\max}}^{(N-1)} \end{pmatrix}. \tag{C12}$$

Here the indices referring to the $l$th cell and the $n$th basis function have been mapped to a single index

$$\alpha(l,n) := (m_{\max}+1)l + n \tag{C13}$$

with

$$\alpha_{\max} = N(m_{\max}+1) - 1. \tag{C14}$$

The original indices may be recovered as

$$n(\alpha) = \alpha \mod (m_{\max}+1), \tag{C15}$$

$$l(\alpha) = (\alpha - n(\alpha))/(m_{\max}+1). \tag{C16}$$

Similarly, we eliminate the dependent coefficients $c_{m_{\max}}^{(l)}$ for $l = 0,\ldots,N-2$ via Eq. (C11) and arrange the remaining independent coefficients into a vector

$$\begin{pmatrix} c_0 \\ c_1 \\ \vdots \\ \vdots \\ \vdots \\ c_{\beta_u} \\ \vdots \\ \vdots \\ \vdots \\ c_{\beta_u^{\max}} \end{pmatrix} = \begin{pmatrix} c_0^{(0)} \\ \vdots \\ c_{m_{\max}-1}^{(0)} \\ c_0^{(1)} \\ \vdots \\ c_{m_{\max}-1}^{(1)} \\ \vdots \\ c_0^{(N-1)} \\ \vdots \\ c_{m_{\max}}^{(N-1)} \end{pmatrix}. \tag{C17}$$

Here the indices referring to the $l$th cell and the $n$th basis function have been mapped to a single index

$$\beta_u(l,n) := m_{\max} l + n, \tag{C18}$$

with

$$\beta_u^{\max} = N m_{\max} + 1. \tag{C19}$$

Based on these indices, we can define the matrix which maps the vector of independent coefficients to a vector of dependent coefficients

$$c_\alpha = \sum_{\beta_u=0}^{\beta_u^{\max}} R_{\alpha,\beta_u} c_{\beta_u}. \tag{C20}$$

These matrices have a very simple structure

$$\begin{pmatrix} 1 & 0 & 0 & & & & & \\ 0 & \ddots & 0 & & & & & \\ 0 & 0 & 1 & & & & & \\ & & 1 & 0 & 0 & & & \\ & & 0 & \ddots & 0 & & & \\ & & 0 & 0 & 1 & & & \\ \vdots & \vdots & \vdots & \vdots & \vdots & \vdots & \vdots & \\ & & & & 1 & & & \\ & & & & & \ddots & & \\ & & & & & & 1 & \end{pmatrix}. \tag{C21}$$

In terms of such matrices, we can define the independent basis functions

$$\chi_{\beta_u}(x) := \sum_{\alpha=0}^{\alpha_{\max}} \chi_\alpha(x) R_{\alpha,\beta_u} \tag{C22}$$

and the wave function in terms of the independent basis functions is given by

$$\psi(x) = \sum_{\beta_u=0}^{\beta_u^{\max}} c_{\beta_u} \chi_{\beta_u}(x). \tag{C23}$$

### 2. Representation of operators

We deal with time-evolution equations of the form

$$\psi'(x') = \int U(x',x)\psi(x)dx, \tag{C24}$$

where $U(x',x)$ denotes an operator $\langle x'|\hat{U}|x\rangle$. We discretize such operators by expressing the wave functions as

$$\psi(x) = \sum_{\beta_u=0}^{\beta_u^{\max}} c_{\beta_u} \chi_{\beta_u}(x), \tag{C25}$$

$$\psi'(x') = \sum_{\beta_u=0}^{\beta_u^{\max}} d_{\beta_u} \chi_{\beta_u}(x') \tag{C26}$$

and testing against independent basis functions $\chi_{\bar{\beta}_u}$. This reduces Eq. (C24) to

$$\sum_{\beta_u=0}^{\beta_u^{\max}} O_{\bar{\beta}_u,\beta_u} d_{\beta_u} = \sum_{\beta_u=0}^{\beta_u^{\max}} U_{\bar{\beta}_u,\beta_u} c_{\beta_u}. \tag{C27}$$

Here $U_{\bar{\beta}_u,\beta_u}$ is the matrix representation of the operator $U(x',x)$ and $O_{\bar{\beta}_u,\beta_u}$ is the overlap matrix.

The matrix representation of $U(x',x)$ is given by

$$U_{\bar{\beta}_u,\beta_u} := \int dx' \int dx\, \chi_{\bar{\beta}_u}(x') U(x',x) \chi_{\beta_u}(x). \tag{C28}$$

This expression can be recast into the form

$$U_{\bar{\beta}_u,\beta_u} := \sum_{\bar{\alpha}=0}^{\alpha_{\max}} \sum_{\alpha=0}^{\alpha_{\max}} R_{\bar{\alpha},\bar{\beta}_u} U_{\bar{\alpha},\alpha} R_{\alpha,\beta_u}, \tag{C29}$$

based on Eq. (C22). Here $U_{\bar{\alpha},\alpha}$ represents the operator $U(x',x)$ projected on the basis set of dependent wave functions

$$U_{\bar{\alpha},\alpha} := \int dx' \int dx\ \chi_{\bar{\alpha}}(x')U(x',x)\chi_{\alpha}(x). \tag{C30}$$

The numerical scheme makes use of three types of matrices: (i) the overlap matrix, (ii) kick-type time-evolution matrices, and (iii) a matrix representation of the free propagator.

(i) The matrix representation of the overlap matrix is

$$O_{\alpha,\bar{\alpha}} = \int dx\ \chi_{\bar{\alpha}}(x)\chi_{\alpha}(x) \tag{C31}$$

$$= \delta_{l(\bar{\alpha}),l(\alpha)} \int dx\ \chi^{l(\alpha)}_{n(\alpha)}(x)\chi^{l(\bar{\alpha})}_{n(\bar{\alpha})}(x) \tag{C32}$$

$$= \delta_{l(\bar{\alpha}),l(\alpha)} \frac{x_{l+1}-x_l}{2} \int_{-1}^{1} dy\ \bar{\chi}_{n(\alpha)}(y)\bar{\chi}_{n(\bar{\alpha})}(y). \tag{C33}$$

The remaining integral can be computed from Eqs. (C6) and (C5). The expression shows that the basis states $\alpha$ and $\bar{\alpha}$ overlap only if they belong to the same cell. Reducing the overlap matrix to independent coefficients according to Eq. (C29) results in a globally connected overlap matrix $O$. The overlap matrix $O$ is real symmetric. Its inverse $O^{-1}$ can be computed by diagonalizing $O$ and inverting its eigenvalues.

(ii) The kick-type time-evolution operators arise as a multiplicative part in Eqs. (48) and (54). We summarize them in a unified form

$$U^V(x,x') = \delta(x-x')\exp\left(-\frac{i}{2\hbar}V(x)\right), \tag{C34}$$

where $V(x)$ denotes either the scaled potential or the kick potential including absorption. Its matrix representation is given by

$$U^V_{\bar{\alpha},\alpha} = \delta_{l(\bar{\alpha}),l(\alpha)} \int dx\ \chi^{l(\alpha)}_{n(\alpha)}(x)\exp\left(-\frac{i}{2\hbar}V(x)\right)\chi^{l(\bar{\alpha})}_{n(\bar{\alpha})}(x). \tag{C35}$$

The remaining integral has to be evaluated numerically, as discussed below. Similar to the overlap matrix, the matrix elements are nonzero only for matrix elements of basis functions in the same cell. The above matrix is reduced to a matrix $U^V$ on independent basis functions according to Eq. (C29). The corresponding coefficients can be propagated via $O^{-1}U^V$, according to Eq. (C27).

(iii) Finally, the matrix representation of propagators corresponding to the free time evolution in between two kicks is given by

$$U^T_{\bar{\alpha},\alpha} = \frac{\exp(i[\theta-\pi/4])}{(2\pi\hbar)^{1/2}} \int dx' \int dx\ \chi^{l(\alpha)}_{n(\alpha)}(x') \times \exp\left(\frac{i}{\hbar}e^{i2\theta}\frac{(x-x')^2}{2}\right)\chi^{l(\bar{\alpha})}_{n(\bar{\alpha})}(x). \tag{C36}$$

The remaining integrals have to be evaluated numerically, as discussed below. The above matrix is reduced to a matrix $U^T$ on independent basis functions according to Eq. (C29). The corresponding coefficients can be propagated via $O^{-1}U^T$, according to Eq. (C27).

Finally, the matrix representation of the full propagator $U$, corresponding to Eqs. (48) or (54), respectively, is given by

$$U = O^{-1}U^V O^{-1}U^T O^{-1}U^V. \tag{C37}$$

Its eigenvalues are obtained from numerical diagonalization.

### 3. Integration

To ensure accurate matrix elements in Eqs. (C35) and (C36), we set the length of the cells such that the integrand does not exhibit more than one oscillation within each cell. We then perform the remaining numerical integration using Gaussian integration with 30–50 integration points (see Ref. [101] for details).

In practice, we estimate the interval $[x,x+\Delta x]$ on which the integrands in Eqs. (C35) and (C36) oscillate once by considering their phase function in the limit of small $\hbar$. This gives

$$\Delta x \simeq \frac{h_{\text{eff}}}{V'(x)}, \tag{C38}$$

$$\Delta x \simeq \frac{h_{\text{eff}}}{|x-x'|}. \tag{C39}$$

Both estimates show that the cell size scales with $h_{\text{eff}}$. Estimating the maximum of $V'(x)$ along the real axis (which is not entirely correct for the scaled potential) from its main part $V_\kappa(q)$, we obtain

$$\max\{V'(x)\} \simeq \frac{\kappa}{4}\exp\left(-\frac{1}{2}\right). \tag{C40}$$

On the other hand, we estimate the maximal relevant length $|x-x'|$ in the integration of Eq. (C36) as

$$\max\{|x-x'|\} \simeq \begin{cases} \sqrt{\frac{30\hbar\log(10)}{\sin(2\theta)}} & \text{(complex scaling)} \\ 2q_{\text{abs}} & \text{(absorbing potentials).} \end{cases} \tag{C41}$$

The first estimate is obtained by computing the separation $|x-x'|$ for which the nonoscillatory part of the kernel in Eq. (C36) drops below machine precision. The second estimate is obtained by assuming that significant contributions in Eq. (C36) arise mainly between points in the absorption-free region $q \in [-q_{\text{abs}},q_{\text{abs}}]$. Usually we have $\max\{|x-x'|\} > \max\{V'(x)\}$ and thus set the number of cells in an equidistant grid to

$$N \approx \frac{1}{h} \times \begin{cases} \sqrt{\frac{30\hbar\log(10)}{\sin(2\theta)}} & \text{(complex scaling)} \\ 2q_{\text{abs}} & \text{(absorbing potentials).} \end{cases} \tag{C42}$$

### 4. Testing

In order to confirm the correctness of the finite-element representation of wave functions, we first applied it to several time-independent problems. These include the box potential, the harmonic oscillator, and the Bain potential, discussed in Ref. [90]. In all cases we could confirm the relevant eigenvalues up to machine precision. This test gives confidence to the

correctness of the overlap matrix as well as the numerical integration routines.

Subsequently, we focus on the matrices $U_V$, deduced from Eq. (C35). Here we test the numerical integrations in Eq. (C35) by comparing to analytical results obtained for simple basis functions. We further tested the matrix $U^V$ by (i) reducing a known wave functions $\psi(x)$ to coefficients, (ii) propagating the coefficients by $O^{-1}U^V$, and (iii) reconstructing the propagated wave function $\psi'(x')$ from the propagated coefficients and noting that the results agree well with the expression $\psi(x)\exp[-iV(x)/2\hbar]$ within the maximum norm.

In a similar way we test the matrix $U_T$, deduced from Eq. (C36). We test the numerical integrations in Eq. (C36) by comparing them to analytical results obtained for simple basis functions. We further tested the matrix $U^T$ by (i) reducing a Gaussian wave function $\psi_g(x)$ to coefficients, (ii) propagating the coefficients by $O^{-1}U^T$, and (iii) reconstructing the propagated wave function $\psi'_g(x',t=1)$ from propagated coefficients and noting that the results agree well within the maximum norm with the closed-form analytical expressions

$$\psi_g(x,t) = \frac{1}{(2\pi)^{1/4}}\frac{\sigma_0^{1/2}}{\sigma_t}\exp\left(-\frac{(x-x_t)^2}{4\sigma_t^2} + i\frac{p_0}{\hbar}(x-x_t) + i\frac{p_0 x_t}{2\hbar}\right), \tag{C43}$$

with

$$x_t = x_0 + p_0 t\exp(-i2\theta), \tag{C44}$$

$$\sigma_t = \sqrt{\sigma_0^2 + \frac{i\hbar}{2}t\exp(-i2\theta)} \tag{C45}$$

obtained when propagating a Gaussian with the complex-scaled propagator (46).

### 5. Complex scaling

The numerical computations for complex scaling in this paper use a grid with $x_{\max} = 4.0$. The order of the basis functions in each cell was $m_{\max} = 10$. The cell width is equidistant. The number of cells was determined as $N = 840$ for the computation with $\theta = 0.05$ and $N = 665$ for $\theta = 0.08$.

All parameters used in this computation were aimed at high accuracy. In particular, further increasing $x_{\max}$, $m_{\max}$, or $N$ does not change the spectra. On the contrary, if resonance spectra are required up to a few significant digits only, the same resonance eigenvalues can be computed for much smaller sets of basis functions $m_{\max}$ and slightly smaller grids $x_{\max}$.

We cross examined the numerical result by computing the spectrum of the complex-scaled quantum map via a quantum maps code, i.e., putting the system on a torus, setting up the operator via a split-operator fast Fourier transform, and computing the spectrum numerically. This gives the same resonance spectrum within several significant digits.

Note that for complex scaling the operator in Eq. (C34) can be amplifying for some positions and damping for others. In the semiclassical limit $\hbar \to 0$ this effects become exponentially amplified, leading to matrix elements in Eq. (C35) which span many orders of magnitude. Eventually, this can make the numerical scheme unstable. If this happens the scaling angle $\theta$ must be lowered.

### 6. Projective opening

The numerical computations with projective openings use basis functions in each cell up to order $m_{\max} = 5$. The cell width is equidistant. The number of cells was determined as $N = 1200$ for the computation with $x_{\max} = 2.0$ and $N = 1500$ for $x_{\max} = 2.5$. In both cases we cannot identify resonance eigenvalues which agree with the results of complex scaling within several significant digits.

The convergence of the spectra was checked, i.e., doubling the number of cells $N$ or the order $m_{\max}$ or both gives the same spectra. Note that treating the projective opening with a quantum map code, i.e., imposing periodic boundary conditions in both position and momentum, gives additional spurious modes.

### 7. Absorbing potential

The numerical computations for absorbing potentials in this paper use basis functions in each cell up to order $m_{\max} = 3$. The cell width is equidistant. The number of cells was determined as $N = 1500$ for the computation with $x_{\max} = 2.5$ and $N = 3000$ for $x_{\max} = 5$. Spectra obtained in the case of weak absorption $x_{\max} = 5.0$ give the same resonance eigenvalues as complex scaling within several significant digits. On the contrary, the case of strong absorbing potentials $x_{\max} = 2.5$ does not agree with resonance eigenvalues obtained from complex scaling. We further checked the convergence of the spectra, i.e., doubling the number of cells $N$ or the order $m_{\max}$ or both gives the same spectra. Note that treating the absorbing potential case with a quantum map code, i.e., imposing periodic boundary conditions in both position and momentum, gives additional spurious modes.

#### *Smooth monomials*

We define the smooth monomials of Sec. IV E as

$$M_n^{\xi}(x) := \xi^n F_n(x/\xi), \tag{C46}$$

where $\xi$ is a width parameter and the functions $F_n(\cdot)$ up to order $n = 3$ are given by

$$F_{-1}(x) = \frac{\exp(-x^2)}{\pi^{1/2}}, \tag{C47}$$

$$F_0(x) = \frac{1}{2}[1 + \mathrm{erf}(x)], \tag{C48}$$

$$F_1(x) = xF_0(x) + \frac{1}{2}F_{-1}(x), \tag{C49}$$

$$F_2(x) = \left(x^2 + \frac{1}{2}\right)F_0(x) + \frac{x}{2}F_{-1}(x), \tag{C50}$$

$$F_3(x) = \left(x^3 + \frac{3x}{2}\right)F_0(x) + \left(\frac{x^2}{2} + \frac{1}{2}\right)F_{-1}(x). \tag{C51}$$

[1] P. Gaspard and S. A. Rice, Scattering from a classically chaotic repellor, J. Chem. Phys. **90**, 2225 (1989).

[2] P. Gaspard and S. A. Rice, Semiclassical quantization of the scattering from a classically chaotic repellor, J. Chem. Phys. **90**, 2242 (1989).

[3] P. Gaspard and S. A. Rice, Exact quantization of the scattering from a classically chaotic repellor, J. Chem. Phys. **90**, 2255 (1989).

[4] R. Blümel and U. Smilansky, A simple model for chaotic scattering: II. Quantum mechanical theory, Physica D **36**, 111 (1989).

[5] R. Blümel and U. Smilansky, Random-Matrix Description of Chaotic Scattering: Semiclassical Approach, Phys. Rev. Lett. **64**, 241 (1990).

[6] C. Jung, Fractal properties in the semiclassical scattering cross section of a classically chaotic system, J. Phys. A **23**, 1217 (1990).

[7] C. Jung and S. Pott, Semiclassical cross section for a classically chaotic scattering system, J. Phys. A **23**, 3729 (1990).

[8] C. Jung and T. Tél, Dimension and escape rate of chaotic scattering from classical and semiclassical cross section data, J. Phys. A **24**, 2793 (1991).

[9] P. Cvitanović and B. Eckhardt, Periodic-Orbit Quantization of Chaotic Systems, Phys. Rev. Lett. **63**, 823 (1989).

[10] G. Tanner, K. Richter, and J.-M. Rost, The theory of two-electron atoms: Between ground state and complete fragmentation, Rev. Mod. Phys. **72**, 497 (2000).

[11] J. Sjöstrand, Geometric bounds on the density of resonances for semiclassical problems, Duke Math. J. **60**, 1 (1990).

[12] K. K. Lin, Numerical study of quantum resonances in chaotic scattering, J. Comput. Phys. **176**, 295 (2002).

[13] W. T. Lu, S. Sridhar, and M. Zworski, Fractal Weyl Laws for Chaotic Open Systems, Phys. Rev. Lett. **91**, 154101 (2003).

[14] H. Schomerus and J. Tworzydło, Quantum-To-Classical Crossover of Quasibound States in Open Quantum Systems, Phys. Rev. Lett. **93**, 154102 (2004).

[15] S. Nonnenmacher, Spectral problems in open quantum chaos, Nonlinearity **24**, R123 (2011).

[16] M. Novaes, Resonances in open quantum maps, J. Phys. A **46**, 143001 (2013).

[17] M. J. Körber, M. Michler, A. Bäcker, and R. Ketzmerick, Hierarchical Fractal Weyl Laws for Chaotic Resonance States in Open Mixed Systems, Phys. Rev. Lett. **111**, 114102 (2013).

[18] J. P. Keating, M. Novaes, S. D. Prado, and M. Sieber, Semiclassical Structure of Chaotic Resonance Eigenfunctions, Phys. Rev. Lett. **97**, 150406 (2006).

[19] M. J. Körber, A. Bäcker, and R. Ketzmerick, Localization of Chaotic Resonance States Due to a Partial Transport Barrier, Phys. Rev. Lett. **115**, 254101 (2015).

[20] S. Nonnenmacher, J. Sjöstrand, and M. Zworski, From open quantum systems to open quantum maps, Commun. Math. Phys. **304**, 1 (2011).

[21] F. Borgonovi, I. Guarneri, and D. L. Shepelyansky, Statistics of quantum lifetimes in a classically chaotic system, Phys. Rev. A **43**, 4517 (1991).

[22] G. Casati, G. Maspero, and D. L. Shepelyansky, Relaxation process in a regime of quantum chaos, Phys. Rev. E **56**, R6233 (1997).

[23] G. Casati, I. Guarneri, and G. Maspero, Fractal Survival Probability Fluctuations, Phys. Rev. Lett. **84**, 63 (2000).

[24] P. Jacquod, H. Schomerus, and C. W. J. Beenakker, Quantum Andreev Map: A Paradigm of Quantum Chaos in Superconductivity, Phys. Rev. Lett. **90**, 207004 (2003).

[25] A. Ossipov, T. Kottos, and T. Geisel, Fingerprints of classical diffusion in open 2D mesoscopic systems in the metallic regime, Europhys. Lett. **62**, 719 (2003).

[26] J. Tworzydło, A. Tajic, H. Schomerus, and C. W. J. Beenakker, Dynamical model for the quantum-to-classical crossover of shot noise, Phys. Rev. B **68**, 115313 (2003).

[27] J. Tworzydło, A. Tajic, and C. W. J. Beenakker, Quantum-to-classical crossover of mesoscopic conductance fluctuations, Phys. Rev. B **69**, 165318 (2004).

[28] J. Tworzydło, A. Tajic, and C. W. J. Beenakker, Weak localization of the open kicked rotator, Phys. Rev. B **70**, 205324 (2004).

[29] S. Nonnenmacher and M. Zworski, Fractal Weyl laws in discrete models of chaotic scattering, J. Phys. A **38**, 10683 (2005).

[30] S. Nonnenmacher and M. Zworski, Distribution of resonances for open quantum maps, Commun. Math. Phys. **269**, 311 (2007).

[31] S. Nonnenmacher and M. Rubin, Resonant eigenstates for a quantized chaotic system, Nonlinearity **20**, 1387 (2007).

[32] J. P. Keating, M. Novaes, and H. Schomerus, Model for chaotic dielectric microresonators, Phys. Rev. A **77**, 013834 (2008).

[33] J. P. Keating, S. Nonnenmacher, M. Novaes, and M. Sieber, On the resonance eigenstates of an open quantum baker map, Nonlinearity **21**, 2591 (2008).

[34] M. Novaes, J. M. Pedrosa, D. Wisniacki, G. G. Carlo, and J. P. Keating, Quantum chaotic resonances from short periodic orbits, Phys. Rev. E **80**, 035202 (2009).

[35] M. Kopp and H. Schomerus, Fractal Weyl laws for quantum decay in dynamical systems with a mixed phase space, Phys. Rev. E **81**, 026208 (2010).

[36] M. Novaes, Supersharp resonances in chaotic wave scattering, Phys. Rev. E **85**, 036202 (2012).

[37] A. Ishii, A. Akaishi, A. Shudo, and H. Schomerus, Weyl law for open systems with sharply divided mixed phase space, Phys. Rev. E **85**, 046203 (2012).

[38] D. Lippolis, J.-W. Ryu, S.-Y. Lee, and S. W. Kim, On-manifold localization in open quantum maps, Phys. Rev. E **86**, 066213 (2012).

[39] M. Schönwetter and E. G. Altmann, Quantum signatures of classical multifractal measures, Phys. Rev. E **91**, 012919 (2015).

[40] N. Mertig, J. Kullig, C. Löbner, A. Bäcker, and R. Ketzmerick, Perturbation-free prediction of resonance-assisted tunneling in mixed regular-chaotic systems, Phys. Rev. E **94**, 062220 (2016).

[41] F. Fritzsch, A. Bäcker, R. Ketzmerick, and N. Mertig, Complex-path prediction of resonance-assisted tunneling in mixed systems, Phys. Rev. E **95**, 020202(R) (2017).

[42] S. Nonnenmacher, J. Sjöstrand, and M. Zworski, Fractal Weyl law for open quantum chaotic maps, arXiv:1105.3128.

[43] H. Schomerus, From scattering theory to complex wave dynamics in non-Hermitian $\mathcal{PT}$-symmetric resonators, Philos. Trans. R. Soc. A **371**, 20120194 (2013).

[44] H. Feshbach, Unified theory of nuclear reactions, Ann. Phys. (NY) **5**, 357 (1958).

[45] H. Feshbach, A unified theory of nuclear reactions. II, Ann. Phys. (NY) **19**, 287 (1962).

[46] I. Rotter, A non-Hermitian Hamilton operator and the physics of open quantum systems, J. Phys. A **42**, 153001 (2009).
[47] C. W. J. Beenakker, Random-matrix theory of quantum transport, Rev. Mod. Phys. **69**, 731 (1997).
[48] Y. V. Fyodorov and H.-J. Sommers, Spectra of random contractions and scattering theory for discrete-time systems, J. Exp. Theor. Phys. Lett. **72**, 422 (2000).
[49] U. V. Riss and H.-D. Meyer, Calculation of resonance energies and widths using the complex absorbing potential method, J. Phys. B **26**, 4503 (1993).
[50] G. Vattay, A. Wirzba, and P. E. Rosenqvist, Periodic Orbit Theory of Diffraction, Phys. Rev. Lett. **73**, 2304 (1994).
[51] I. Březinová, L. Wirtz, S. Rotter, C. Stampfer, and J. Burgdörfer, Transport through open quantum dots: Making semiclassics quantitative, Phys. Rev. B **81**, 125308 (2010).
[52] F. Lackner, I. Březinová, J. Burgdörfer, and F. Libisch, Semiclassical wave functions for open quantum billiards, Phys. Rev. E **88**, 022916 (2013).
[53] J. Aguilar and J. M. Combes, A class of analytic perturbations for one-body Schrödinger Hamiltonians, Commun. Math. Phys. **22**, 269 (1971).
[54] E. Balslev and J. M. Combes, Spectral properties of many-body Schrödinger operators with dilatation-analytic interactions, Commun. Math. Phys. **22**, 280 (1971).
[55] M. Reed and B. Simon, *Methods of Modern Mathematical Physic IV: Analysis of Operators* (Academic, New York, 1978).
[56] W. P. Reinhardt, Complex coordinates in the theory of atomic and molecular structure and dynamics, Annu. Rev. Phys. Chem. **33**, 223 (1982).
[57] N. Moiseyev, Quantum theory of resonances: calculating energies, widths and cross-sections by complex scaling, Phys. Rep. **302**, 212 (1998).
[58] S.-I. Chu and W. P. Reinhardt, Intense Field Multiphoton Ionization Via Complex Dressed States: Application to the H Atom, Phys. Rev. Lett. **39**, 1195 (1977).
[59] A. Maquet, S.-I. Chu, and W. P. Reinhardt, Stark ionization in dc and ac fields: An $l^2$ complex-coordinate approach, Phys. Rev. A **27**, 2946 (1983).
[60] N. Moiseyev and H. J. Korsch, Metastable quasienergy positions and widths for time-periodic Hamiltonians by the complex-coordinate method, Phys. Rev. A **41**, 498 (1990).
[61] N. Ben-Tal, N. Moiseyev, C. Leforestier, and R. Kosloff, Positions, lifetimes, and partial widths of metastable quasienergy states by solving the time-dependent complex-scaled schrödinger equation, J. Chem. Phys. **94**, 7311 (1991).
[62] N. Ben-Tal, N. Moiseyev, R. Kosloff, and C. Cerjan, Harmonic generation in ionizing systems by the time-dependent complex coordinate Floquet method, J. Phys. B **26**, 1445 (1993).
[63] R. S. MacKay, J. D. Meiss, and I. C. Percival, Stochasticity and Transport in Hamiltonian Systems, Phys. Rev. Lett. **52**, 697 (1984).
[64] R. S. Mackay, J. D. Meiss, and I. C. Percival, Transport in Hamiltonian systems, Physica D **13**, 55 (1984).
[65] V. Rom-Kedar, Transport rates of a class of two-dimensional maps and flows, Physica D **43**, 229 (1990).
[66] S. Wiggins, *Chaotic Transport in Dynamical Systems*, Interdisciplinary Applied Mathematics Vol. 2 (Springer, New York, 1992).
[67] V. Rom-Kedar, Homoclinic tangles-classification and applications, Nonlinearity **7**, 441 (1994).
[68] K. A. Mitchell, J. P. Handley, B. Tighe, A. Flower, and J. B. Delos, Chaos-Induced Pulse Trains in the Ionization of Hydrogen, Phys. Rev. Lett. **92**, 073001 (2004).
[69] K. A. Mitchell, J. P. Handley, B. Tighe, A. Flower, and J. B. Delos, Analysis of chaos-induced pulse trains in the ionization of hydrogen, Phys. Rev. A **70**, 043407 (2004).
[70] K. Burke, K. A. Mitchell, B. Wyker, S. Ye, and F. B. Dunning, Demonstration of Turnstiles as a Chaotic Ionization Mechanism in Rydberg Atoms, Phys. Rev. Lett. **107**, 113002 (2011).
[71] M. J. Davis and S. K. Gray, Unimolecular reactions and phase space bottlenecks, J. Chem. Phys. **84**, 5389 (1986).
[72] B. Eckhardt, Fractal properties of scattering singularities, J. Phys. A **20**, 5971 (1987).
[73] M. V. Berry, N. L. Balazs, M. Tabor, and A. Voros, Quantum maps, Ann. Phys. (NY) **122**, 26 (1979).
[74] G. Casati, B. Chirikov, F. Izrailev, and J. Ford, Stochastic behavior of a quantum pendulum under a periodic perturbation, in *Stochastic Behavior in Classical and Quantum Hamiltonian Systems*, edited by G. Casati and J. Ford, Lecture Notes in Physics Vol. 334 (Springer, Berlin, 1979).
[75] J. H. Jensen, Quantum corrections for chaotic scattering, Phys. Rev. A **45**, 8530 (1992).
[76] J. H. Jensen, Accuracy of the semiclassical approximation for chaotic scattering, Phys. Rev. E **51**, 1576 (1995).
[77] Y. Krivolapov, S. Fishman, E. Ott, and T. M. Antonsen, Quantum chaos of a mixed open system of kicked cold atoms, Phys. Rev. E **83**, 016204 (2011).
[78] T. Onishi, A. Shudo, K. S. Ikeda, and K. Takahashi, Tunneling mechanism due to chaos in a complex phase space, Phys. Rev. E **64**, 025201(R) (2001).
[79] T. Onishi, A. Shudo, K. S. Ikeda, and K. Takahashi, Semiclassical study on tunneling processes via complex-domain chaos, Phys. Rev. E **68**, 056211 (2003).
[80] B. V. Chirikov, A universal instability of many-dimensional oscillator systems, Phys. Rep. **52**, 263 (1979).
[81] S. Smale, Dynamical systems and the topological conjugacy problem for diffeomorphisms, in *Proceedings of the International Congress of Mathematicians, Stockholm, 1962* (Mittag-Leffler Institute, Djursholm, 1962), p. 490.
[82] S. Wiggins, *Introduction to Applied Nonlinear Dynamical Systems and Chaos*, Texts in Applied Mathematics Vol. 2 (Springer, New York, 2003).
[83] G. Floquet, Sur les équations différentielles linéaires á coefficients périodiques, Ann. Sci. École Norm. S. Ser. 2 **12**, 47 (1883).
[84] H. Sambe, Steady states and quasienergies of a quantum-mechanical system in an oscillating field, Phys. Rev. A **7**, 2203 (1973).
[85] K. Yajima, Resonances for the ac-Stark effect, Commun. Math. Phys. **87**, 331 (1982).
[86] S. Graffi and K. Yajima, Exterior complex scaling and the ac-Stark effect in a Coulomb field, Commun. Math. Phys. **89**, 277 (1983).
[87] J. S. Howland, Complex scaling of ac Stark Hamiltonians, J. Math. Phys. **24**, 1240 (1983).
[88] B. Simon, Resonances in $n$-body quantum systems with dilatation analytic potentials and the foundations of time-dependent perturbation theory, Ann. Math. **97**, 247 (1973).
[89] B. Simon, Resonances and complex scaling: A rigorous overview, Int. J. Quantum Chem. **14**, 529 (1978).

[90] A. Scrinzi and N. Elander, A finite element implementation of exterior complex scaling for the accurate determination of resonance energies, J. Chem. Phys. **98**, 3866 (1993).

[91] A. Scrinzi, Infinite-range exterior complex scaling as a perfect absorber in time-dependent problems, Phys. Rev. A **81**, 053845 (2010).

[92] U. Peskin and N. Moiseyev, Time-independent scattering theory for time-periodic Hamiltonians: Formulation and complex-scaling calculations of above-threshold-ionization spectra, Phys. Rev. A **49**, 3712 (1994).

[93] G. Tanner, K. T. Hansen, and J. Main, The semiclassical resonance spectrum of hydrogen in a constant magnetic field, Nonlinearity **9**, 1641 (1996).

[94] J. A. Ramilowski, S. D. Prado, F. Borondo, and D. Farrelly, Fractal Weyl law behavior in an open Hamiltonian system, Phys. Rev. E **80**, 055201 (2009).

[95] H. Friedrich and D. Wintgen, The hydrogen atom in a uniform magnetic field—An example of chaos, Phys. Rep. **183**, 37 (1989).

[96] A. Buchleitner, B. Grémaud, and D. Delande, Wavefunctions of atomic resonances, J. Phys. B **27**, 2663 (1994).

[97] J. Zakrzewski, D. Delande, and A. Buchleitner, Ionization via chaos assisted tunneling, Phys. Rev. E **57**, 1458 (1998).

[98] A. Buchleitner, D. Delande, and J. Zakrzewski, Non-dispersive wave packets in periodically driven quantum systems, Phys. Rep. **368**, 409 (2002).

[99] D. Delande and J. Zakrzewski, Experimentally attainable example of chaotic tunneling: The hydrogen atom in parallel static electric and magnetic fields, Phys. Rev. A **68**, 062110 (2003).

[100] J. P. Eckmann and D. Ruelle, Ergodic theory of chaos and strange attractors, Rev. Mod. Phys. **57**, 617 (1985).

[101] J. Stoer and R. Bulirsch, *Introduction to Numerical Analysis*, 3rd ed. (Springer, New York, 2002), Vol. 12, Chap. 3.6.